Commun. Comput. Phys.
doi: 10.4208/cicp.061113.050115a

Vol. **18**, No. 2, pp. 380-416
August 2015

Numerical Simulations of Particle Sedimentation Using the Immersed Boundary Method

Sudeshna Ghosh[1] and John M. Stockie[1,*]

[1] *Department of Mathematics, Simon Fraser University, Burnaby, British Columbia, V5A 1S6, Canada.*

Received 6 November 2013; Accepted (in revised version) 5 January 2015

Abstract. We study the settling of solid particles in a viscous incompressible fluid contained within a two-dimensional channel, where the mass density of the particles is greater than that of the fluid. The fluid-structure interaction problem is simulated numerically using the immersed boundary method, where the added mass is incorporated using a Boussinesq approximation. Simulations are performed with a single circular particle, and also with two particles in various initial configurations. The terminal particle settling velocity and drag coefficient correspond closely with other theoretical, experimental and numerical results, and the particle trajectories reproduce the expected behavior qualitatively. In particular, simulations of a pair of interacting particles similar drafting-kissing-tumbling dynamics to that observed in other experimental and numerical studies.

AMS subject classifications: 45K05, 74F10, 76D05, 76M20, 76T20

Key words: Immersed boundary method, particle suspension, sedimentation, settling velocity, fluid-structure interaction.

1 Introduction

Particulate flows involve the interaction of a dynamically evolving fluid with solid suspended particles, and arise in a wide range of applications in natural and industrial processes [10]. We are particularly interested in the gravitational settling or sedimentation problem, in which the suspended particles settle under their own weight. Sedimentation is observed in many applications including flow of pollutants in rivers and the atmosphere, tea leaves settling in a teacup, industrial crystal precipitation, mineral ore processing, and hail formation in thunderclouds to name just a few.

There is an extensive literature on experimental, theoretical and computational studies of particulate flows. We will not attempt to provide a comprehensive review here, but

*Corresponding author. *Email addresses:* sud1800@yahoo.co.in (S. Ghosh), jstockie@sfu.ca (J. M. Stockie)

 ©2015 Global-Science Press

https://doi.org/10.4208/cicp.061113.050115a Published online by Cambridge University Press

will rather highlight a few of the more important results. Experimental studies of sedimentation have had a long history including the early work of Richardson and Zaki [40] and extending to more recent years [15,19,27,28]. Many analytical and approximate solutions have been developed that capture the behavior of settling suspensions, especially in the dilute limit where there are only a small number of particles. Back in 1851, Stokes [43] derived an analytical solution for a single particle settling within an unbounded fluid, and many other authors have since extended these results to other more practical sedimentation problems [7, 14, 47]. More recently, many numerical approaches have been developed to simulate settling particles, including the finite element [18, 21, 35], lattice-Boltzmann [16, 31], and boundary element methods [25, 38]. The common feature in all of these approaches is that the fluid flow is governed by the Navier-Stokes equations whereas the particles are governed by Newton's equations of motion. The hydrodynamic forces between the particle and fluid are obtained from the solution of this coupled system, which typically requires either complex interfacial matching conditions at the fluid-particle interface or else some form of dynamic boundary-fitted meshing. In any case, these methods tend to be complex and extremely CPU-intensive, especially for three-dimensional problems.

One numerical approach that has proven to be especially effective for solving complex fluid-structure interaction problems involving dynamic moving structures is the *immersed boundary* (or IB) method. This approach has been used extensively to simulate deformable structures arising from problems in biofluid mechanics [37]. For example, Wang and Layton [48] have used the IB method to simulate sedimentation of multiple rigid 1D fibers suspended in a viscous incompressible fluid, while several other authors have applied the IB approach to solve related sedimentation problems [8, 16, 26, 46, 49].

The IB method is a mixed Eulerian-Lagrangian approach in which the fluid equations are solved on an equally-spaced rectangular mesh, while the moving boundaries are approximated at a set of points that moves relative to the underlying fluid grid. In the original IB method, the effect of these immersed boundaries is represented as a singular force that is computed from the current IB configuration and spread onto fluid grid points by means of a regularized delta function. The added mass due to a sedimenting particle can be distributed onto the fluid in a similar manner. With the exception of the papers by Wang and Layton [48] and Hopkins and Fauci [26], the other authors mentioned above have employed a modification of this IB approach known as the "direct forcing IB method." In this approach the force instead takes the role of a Lagrange multiplier that is chosen to constrain the fluid and structure to move with the same velocity (see [34] for more details). The direct forcing method has the advantage that it resolves the immersed structure sharply and avoids the sometimes severe time step restriction arising from very stiff springs; on the other hand, it is also considerably more complicated to implement, especially when the immersed boundary is moving.

Our aim in this paper is apply the original IB method rather than the direct forcing approach to solving sedimentation problems. We restrict ourselves to a two-dimensional geometry in which one or two particles with circular cross-section settle under the influ-

https://doi.org/10.4208/cicp.061113.050115a Published online by Cambridge University Press

ence of gravity within a rectangular channel having vertical bounding walls. Although the IB approach has been applied to solve certain sedimentation problems, there has not yet been an extensive comparison to other results in the literature. Our primary aim is therefore to perform such a comparison with a number of experimental [44, 50], theoretical [17, 45], and numerical [18] studies, in order to ascertain the validity of the IB approach in simulating sedimentation problems. Although we focus here on rigid particles, the long-term goal of our work is to develop a numerical framework that can be applied to the settling of highly deformable particles.

We begin in Section 2 by describing the IB method and the forces used to simulate the presence of both particles and channel walls. Section 3 contains a review of previous analytical and experimental results on the settling velocity of a single particle in unbounded and wall-bounded domains. We then perform a series of numerical simulations of sedimentation at small to moderate Reynolds numbers and report the results in Sections 4 and 5. Most of the results appearing in this article are contained in the PhD thesis of the first author [20].

2 Immersed boundary method

2.1 Model formulation

The immersed boundary method is both a mathematical formulation and a numerical scheme. We begin in this section by describing the model equations that underlie the IB formulation for capturing the fluid-structure interaction between solid elastic bodies of general shape that move within a surrounding incompressible, Newtonian fluid under the action of gravitational force. The details of the IB force density used to handle a solid circular object in the presence of two parallel bounding walls are left for Section 2.3. All variables and parameters in this paper are stated in CGS units unless otherwise indicated.

Suppose that a moving elastic solid body Γ is contained within a fluid domain Ω as pictured in Fig. 1. In general, Γ may consist of several disconnected components, $\Gamma = \bigcup_i \Gamma_i$, where each Γ_i can be either a 1D elastic membrane (parameterized by a single real parameter s) or an elastic solid region (whose specification requires two parameters, r and s). We denote the location or "configuration" of the immersed boundary by $\boldsymbol{x}=\boldsymbol{X}(\boldsymbol{q},t)$ [cm], where $\boldsymbol{q}$ is a dimensionless parameterization that represents either a scalar s or a vector (r,s) depending on the context, and $\boldsymbol{x}=(x,y)$ are Eulerian coordinates. The fluid domain $\Omega=[0,L_x]\times[0,L_y]$ is rectangular in shape and periodic boundary conditions are applied in both the x- and y-directions.

The effect of the elastic body on the fluid is to impose a force $\boldsymbol{f}_{IB}$ [g/cm^{2}s^2] onto the adjacent fluid particle at location $\boldsymbol{x}=\boldsymbol{X}(\boldsymbol{q},t)$, which is incorporated in the incompressible Navier-Stokes equations as follows:

$$\rho\frac{\partial \boldsymbol{u}}{\partial t}+\rho\boldsymbol{u}\cdot\nabla\boldsymbol{u}=\mu\nabla^2\boldsymbol{u}-\nabla p+\boldsymbol{f}_{IB}, \tag{2.1}$$

https://doi.org/10.4208/cicp.061113.050115a Published online by Cambridge University Press

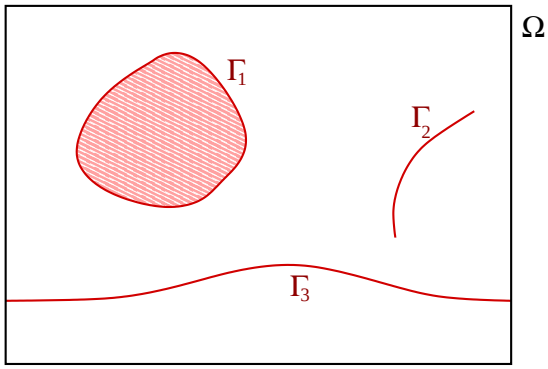


Figure 1: A general immersed boundary configuration $\Gamma=\bigcup_{i=1}^{3}\Gamma_i$ consisting of several disconnected components immersed within a doubly-periodic fluid domain Ω.

$$\nabla\cdot\boldsymbol{u}=0. \tag{2.2}$$

Here, $\boldsymbol{u}(\boldsymbol{x},t)$ is the fluid velocity [cm/s], $p(\boldsymbol{x},t)$ is pressure [g/cms^2], ρ is density [g/cm^3], and μ is dynamic viscosity [g/cms]. The IB forcing term in (2.1) is represented by a force density $\boldsymbol{F}_{IB}(\boldsymbol{q},t)$ [g/s^2] that is spread onto the surrounding fluid by means of a delta-function convolution

$$\boldsymbol{f}_{IB}(\boldsymbol{x},t)=\int_{\Gamma}\boldsymbol{F}_{IB}(\boldsymbol{q},t)\delta(\boldsymbol{x}-\boldsymbol{X}(\boldsymbol{q},t))\,d\boldsymbol{q}, \tag{2.3}$$

where $\delta(\boldsymbol{x})=\delta(x)\delta(y)$ is the Cartesian product of two 1D Dirac delta functions. The consistency of the above equations with the dynamics of an actual incompressible elastic material interacting with an incompressible fluid is demonstrated under general conditions in [37].

Most papers in the immersed boundary literature assume that Γ has the same constant density ρ_f as the surrounding fluid, and hence Γ is neutrally buoyant. However, for the particle sedimentation application considered here, we must take Γ (or at least portions of it) to have density $\rho_s>\rho_f$ that is greater than that of the fluid. Consequently, the density of the fluid-solid composite material is $\rho(\boldsymbol{x},t)=\rho_f+\Delta\rho(\boldsymbol{x},t)$, where the added mass may also be written in terms of a delta function convolution as [52]

$$\Delta\rho(\boldsymbol{x},t)=\int_{\Gamma}M(\boldsymbol{q})\delta(\boldsymbol{x}-\boldsymbol{X}(\boldsymbol{q},t))\,d\boldsymbol{q}.$$

The quantity $M(\boldsymbol{q})\geqslant 0$ is the added Lagrangian mass density due to Γ, with $M=0$ only for those components that are neutrally buoyant.

In all examples in this paper, we take $M\equiv M_o$ (constant) and assume that the solid density is close to that of the fluid, so that $\Delta\rho\ll\rho_f$. Consequently, it is reasonable to apply a Boussinesq approximation [26] in which the extra intertial term involving $\Delta\rho$ is neglected and the density on the left hand side of the momentum equations (2.1) is equal

https://doi.org/10.4208/cicp.061113.050115a Published online by Cambridge University Press

to the constant ρ_f:

$$\rho_f \frac{\partial \boldsymbol{u}}{\partial t} + \rho_f \boldsymbol{u} \cdot \nabla \boldsymbol{u} = \mu \nabla^2 \boldsymbol{u} - \nabla p + \boldsymbol{f}_{IB} + \boldsymbol{f}_G. \tag{2.4}$$

The forcing term $\boldsymbol{f}_G$ derives from the force of gravity acting on the immersed boundary and can be written as [26]

$$\boldsymbol{f}_G(\boldsymbol{x},t) = -g\hat{k}\Delta\rho = -g\hat{k}\int_\Gamma M(\boldsymbol{q})\delta(\boldsymbol{x}-\boldsymbol{X}(\boldsymbol{q},t))\,d\boldsymbol{q}, \tag{2.5}$$

where $g = 980$ cm/s^2 is the gravitational acceleration and $\hat{k} = (0,1)$ is the vertical unit vector. Finally, the immersed boundary is assumed to move according to

$$\frac{\partial \boldsymbol{X}}{\partial t} = \int_\Omega \boldsymbol{u}(\boldsymbol{x},t)\delta(\boldsymbol{x}-\boldsymbol{X}(\boldsymbol{q},t))\,d\boldsymbol{x}, \tag{2.6}$$

which is simply the "no-slip" condition.

In summary, the governing equations consist of (2.2), (2.4)-(2.6), with the IB force density being the only component that remains to be specified. Since it is easiest to write $\boldsymbol{f}_{IB}$ in discrete form, we will first derive the discretized governing equations, after which we will provide a specification for the IB force.

2.2 Numerical algorithm

We employ a semi-implicit scheme that is closely related to the method detailed in [41]. The fluid domain Ω is divided into an equally-spaced grid of points $\boldsymbol{x}_{i,j} = (x_i, y_j) = (ih_x, jh_y)$ with $h_x = L_x/N_x$, $h_y = L_y/N_y$, $i = 1,2,\cdots,N_x$, and $j = 1,2,\cdots,N_y$. The time interval $[0,T]$ is divided into equally-spaced points $t_n = n\Delta t$ with time step $\Delta t = T/N_t$ and $n = 0,1,2,\cdots,N_t$. Discrete approximations of the velocity and pressure are then given by $\boldsymbol{u}_{i,j}^n$ and $p_{i,j}^n$ at points (x_i, y_j, t_n). The immersed boundary Γ is similarly discretized at points $\boldsymbol{X}_\ell$ for $\ell = 1,2,\cdots,N_b$, and the IB location and force density are denoted $\boldsymbol{X}_\ell^n$ and $\boldsymbol{F}_\ell^n$ respectively.

Using the above notation, we can then introduce difference operators that approximate spatial derivatives appearing in the governing equations. In particular, we define two one-sided approximations of the x–derivative of a grid quantity $w_{i,j}$

$$D_x^+ w_{i,j} = \frac{w_{i+1,j} - w_{i,j}}{h_x} \quad \text{and} \quad D_x^- w_{i,j} = \frac{w_{i,j} - w_{i-1,j}}{h_x}, \tag{2.7}$$

as well as the centered approximation

$$D_x^0 w_{i,j} = \frac{w_{i+1,j} - w_{i-1,j}}{2h_x}. \tag{2.8}$$

https://doi.org/10.4208/cicp.061113.050115a Published online by Cambridge University Press

Analogous definitions apply for the y–derivative approximations D_y^+, D_y^- and D_y^0, and the gradient is replaced by the centered approximation $\nabla_h = (D_x^0, D_y^0)$. Finally, the delta function is replaced by the regularized function

$$\delta_h(\boldsymbol{x}) = \frac{1}{h_x h_y}\phi\left(\frac{x}{h_x}\right)\phi\left(\frac{y}{h_y}\right), \quad \text{where} \quad \phi(r) = \begin{cases} \frac{1}{4}\left(1+\cos\left(\frac{\pi r}{2}\right)\right), & \text{if } |r| \leqslant 2, \\ 0, & \text{otherwise.} \end{cases} \tag{2.9}$$

We are now prepared to state the immersed boundary algorithm, which evolves values of velocity $\boldsymbol{u}_{i,j}^{n-1}$ and IB configuration $\boldsymbol{X}_\ell^{n-1}$ at the previous step to time t_n using the following procedure:

1. Compute the IB force density $\boldsymbol{F}_{IB,\ell}^{n-1}$ based on $\boldsymbol{X}_\ell^{n-1}$ as described in Section 2.3.

2. Spread the IB force to fluid grid points using a discretization of the integral (2.3)

$$\boldsymbol{f}_{IB,i,j}^{n-1} = \sum_{\ell=1}^{N_b} \boldsymbol{F}_{IB,\ell}^{n-1}\,\delta_h(\boldsymbol{x}_{i,j} - \boldsymbol{X}_\ell^{n-1})\,A_b. \tag{2.10}$$

   An analogous approximation of the integral in (2.5) yields a formula for $\boldsymbol{f}_{G,i,j}^{n-1}$. The scaling factor A_b in both cases is inversely proportional to the number of IB points (N_b), whose value depends on whether the immersed boundary is a 1D fiber (channel wall) or 2D solid region (circular particle). In the case of a fiber A_b is a length, while for a solid region A_b is an area; in both cases, the factor A_b ensures that the formula (2.10) scales properly with the number of IB points and that it is a consistent approximation of the corresponding integral. More details on the precise form of (2.10) and A_b are provided in Section 2.3.

3. Integrate the incompressible Navier-Stokes equations using a projection scheme:

   (a) Compute an intermediate velocity $\boldsymbol{u}_{i,j}^{(1)}$ by applying the elastic and gravitational forces to the immersed boundary:

$$\rho_f\left(\frac{\boldsymbol{u}_{i,j}^{(1)} - \boldsymbol{u}_{i,j}^{n-1}}{\Delta t}\right) = \boldsymbol{f}_{IB,i,j}^{n-1} + \boldsymbol{f}_{G,i,j}^{n-1}. \tag{2.11}$$

   (b) Apply an ADI discretization of the advection and diffusion terms

$$\rho_f\left(\frac{\boldsymbol{u}_{i,j}^{(2)} - \boldsymbol{u}_{i,j}^{(1)}}{\Delta t} + u_{i,j}^{n-1} D_x^0 \boldsymbol{u}_{i,j}^{(2)}\right) = \mu D_x^+ D_x^- \boldsymbol{u}_{i,j}^{(2)}, \tag{2.12}$$

$$\rho_f\left(\frac{\boldsymbol{u}_{i,j}^{(3)} - \boldsymbol{u}_{i,j}^{(2)}}{\Delta t} + v_{i,j}^{n-1} D_y^0 \boldsymbol{u}_{i,j}^{(3)}\right) = \mu D_y^+ D_y^- \boldsymbol{u}_{i,j}^{(3)}, \tag{2.13}$$

   which represent a sequence of tridiagonal solves for $\boldsymbol{u}_{i,j}^{(2)}$ and $\boldsymbol{u}_{i,j}^{(3)}$.

https://doi.org/10.4208/cicp.061113.050115a Published online by Cambridge University Press

(c) Project the velocity $\boldsymbol{u}_{i,j}^{(3)}$ onto the space of divergence-free vector fields by:

i. Solving the pressure Poisson equation

$$\nabla_h \cdot \nabla_h p_{i,j} = \frac{\rho_f}{\Delta t} \nabla_h \boldsymbol{u}_{i,j}^{(3)}. \tag{2.14}$$

Note that $\nabla_h \cdot \nabla_h$ represents a wide finite difference stencil for the Laplacian involving the pressure values $p_{i,j}$, $p_{i-2,j}$, $p_{i+2,j}$, $p_{i,j-2}$ and $p_{i,j+2}$. Owing to the periodic boundary conditions on Ω, the resulting system of linear equations is solved most easily by means of the discrete Fourier transform, which is calculated using the Fast Fourier Transform (FFT) algorithm.

ii. Updating the velocity according to

$$\boldsymbol{u}_{i,j}^{n} = \boldsymbol{u}_{i,j}^{(3)} - \frac{\Delta t}{\rho_f} \nabla_h p_{i,j}. \tag{2.15}$$

4. Evolve the immersed boundary using

$$\boldsymbol{X}_{\ell}^{n} = \boldsymbol{X}_{\ell}^{n-1} + \Delta t \sum_{i,j} \boldsymbol{u}_{i,j}^{n} \delta_h(\boldsymbol{x}_{i,j} - \boldsymbol{X}_{\ell}^{n-1}) h_x h_y. \tag{2.16}$$

This simple semi-implicit scheme imposes a CFL-type time-step restriction that depends on the Reynolds number as well as the elastic IB force. The dependence of the stable time step on parameters can be characterized in certain idealized cases [6,32], and these results can be used as a guide to selecting a value for Δt, but in practical computations the time step must be determined manually.

This algorithm yields a solution that is first-order accurate in time, and although all spatial derivatives are approximated using second-order finite differences, the spatial accuracy reduces to first order owing to the fact that we are approximating a sharp interface with a non-smooth velocity field and discontinuous pressure. It is straightforward to increase the temporal accuracy to second order using an algorithm such as that proposed by Lai and Peskin [33], but it is much more difficult to increase spatial accuracy without implementing a much more complicated approach such as local adaptive mesh refinement [22]. Since the focus of the current study is to validate the general IB approach in the study of particle sedimentation, we have chosen to employ the simple first-order scheme above.

2.3 Discrete IB force density for particle and channel walls

The geometry of the particle sedimentation problem is depicted in Fig. 2, where a rectangular fluid domain of size $L_x \times L_y$ contains two vertical channel walls set a distance $W < L_x$ apart. The walls are placed symmetrically about the channel centerline and are separated from the domain boundary by a narrow strip of fluid. Periodic boundary conditions are

https://doi.org/10.4208/cicp.061113.050115a Published online by Cambridge University Press

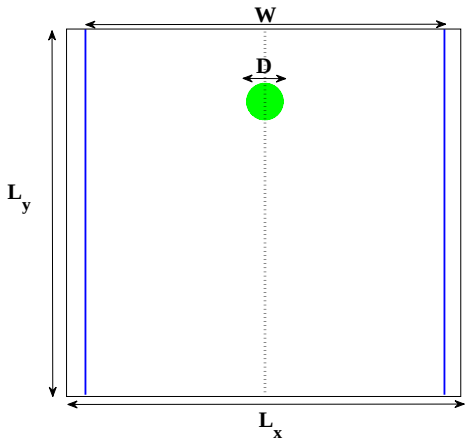


Figure 2: Initial geometry for the single-particle settling problem. The parallel channel walls are separated by a distance W and contain a particle of diameter D located along the channel centerline (shown as a dotted line).

applied on all sides so that the channel walls naturally connect to each other across the top and bottom boundaries. A single, solid, circular particle of diameter D is initially located at the center of the channel. Later on, we will consider other initial configurations with one and two particles, but for now this will suffice to illustrate the calculation of the IB force. The IB force density $\boldsymbol{F}_{IB}$ is the sum of two terms, $\boldsymbol{F}_{IB}=\boldsymbol{F}^w+\boldsymbol{F}^c$, where $\boldsymbol{F}^w$ represents the force density generated by the channel walls and $\boldsymbol{F}^c$ is that generated by the circular particle. These forces are discussed separately in the next two sections.

2.3.1 Elastic force from the channel walls, $\boldsymbol{F}^w$

The vertical walls are discretized at an array of equally-spaced points that are initially at locations $\boldsymbol{X}_\ell^{w,L}=\left(\frac{1}{2}(L_x-W),\ell h_w\right)$ for the left wall and $\boldsymbol{X}_\ell^{w,R}=\left(\frac{1}{2}(L_x+W),\ell h_w\right)$ for the right wall, with point spacing $h_w=L_y/N_w$ and $\ell=1,2,\cdots,N_w$. Each IB point is connected to a fixed "tether point" (initially at the same location) by a very stiff spring that exerts a force

$$\boldsymbol{F}_\ell^{w,L}=\sigma_w(\boldsymbol{X}_\ell^{w,L}-\boldsymbol{X}_\ell), \tag{2.17}$$

where σ_w [g/cms^2] is the spring stiffness and $\boldsymbol{X}_\ell$ is the moving IB point location. Whenever an IB point departs from the corresponding tether point location, a force is generated that drives it back towards the target, so that if σ_w is chosen large enough the wall points can be made to mimic a rigid structure. We emphasize that tether points neither move with the fluid nor generate any force themselves. A similar expression is developed for the right wall points $\boldsymbol{F}_\ell^{w,R}$, so that the total wall force density is

$$\boldsymbol{F}^w=\sum_{\ell=1}^{N_w}(\boldsymbol{F}_\ell^{w,L}+\boldsymbol{F}_\ell^{w,R}). \tag{2.18}$$

https://doi.org/10.4208/cicp.061113.050115a Published online by Cambridge University Press

The natural choice of scaling factor in the force spreading step (2.10) is the wall point spacing, $A_b = h_w$.

2.3.2 Elastic force from the particle, $\boldsymbol{F}^c$

The circular particle is represented by N_c Lagrangian points lying on its circumference and throughout its interior. We employ the unstructured triangular mesh code DistMesh [36] that generates a nearly uniform triangulation such as in Fig. 3. The nodes of the triangulation are the IB points $\boldsymbol{X}_\ell$ for $\ell = 1,2,\cdots,N_c$, while the edges define the spring network that maintains the particle shape. In addition to bearing IB spring forces, the network nodes are also employed in Eq. (2.5) to distribute the added particle mass. In practice, we generate a triangulation using the Matlab function `distmesh2d` with "scaled edge length function" `huniform` (which attempts to find a mesh that is as close to uniform as possible). We also set the "initial edge length" parameter equal to $\frac{1}{3}\min(h_x,h_y)$, which ensures that the mesh obeys

$$\max_{k,\ell} |\boldsymbol{X}_k - \boldsymbol{X}_\ell| < \frac{1}{2}\min(h_x,h_y),$$

which is a standard "rule of thumb" that avoids leakage of fluid between IB points [37].

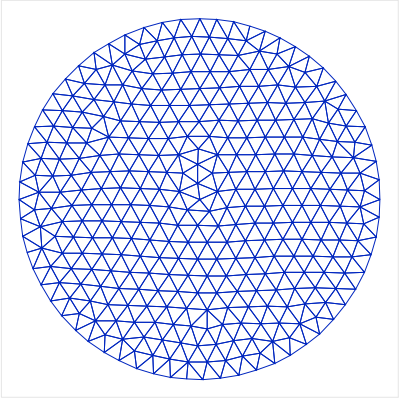


Figure 3: Uniform triangular mesh generated by `distmesh2d`.

Our particle discretization should be compared with the more common IB approach of taking an open circular ring inside which is a freely-moving fluid [33, 49]. This approach has been criticized [23] for generating non-physical fluid motions inside the particle, which in some cases leads to significant deviations in the particle shape. In contrast, our IB spring network discretization suppresses this spurious fluid motion and maintains the circular shape of the particle.

We now define the spring forces acting on the network, following the development of Alpkvist and Klapper for viscoelastic biofilm structures [2]. Let $\boldsymbol{d}_{\ell,m}(t) = \boldsymbol{X}_\ell(t) - \boldsymbol{X}_m(t)$ be the vector joining two IB points ℓ and m, and let $d_{\ell,m}(t) = |\boldsymbol{d}_{\ell,m}(t)|$ be the corresponding distance. We assume that the spring network is initially in equilibrium and take all

https://doi.org/10.4208/cicp.061113.050115a Published online by Cambridge University Press

springs to have a resting length equal to their initial length, $d_{\ell,m}(0)$. Let $\mathbb{I}$ be an incidence matrix with entries $\mathbb{I}_{\ell,m}$ equal to either 1 or 0 depending on whether points ℓ and m are connected or not, respectively. The force density acting on the ℓ^{th} IB point is

$$\boldsymbol{F}_\ell^c = \sigma_c \sum_{\substack{m=1 \\ \mathbb{I}_{\ell,m}\neq 0}}^{N_b} \mathbb{I}_{\ell,m} \frac{\boldsymbol{d}_{\ell,m}}{d_{\ell,m}} (d_{\ell,m}(0) - d_{\ell,m}), \tag{2.19}$$

where the sum is taken only over those m for which $\boldsymbol{X}_m$ is connected to $\boldsymbol{X}_\ell$. We assume that the spring stiffness σ_c [g/cms^2] is constant for all network connections. The total elastic force density generated by all IB points making up the particle is then

$$\boldsymbol{F}^c = \sum_{\ell=1}^{N_c} \boldsymbol{F}_\ell^c. \tag{2.20}$$

The appropriate scaling factor for the force integral (2.10) is the average area of a triangular mesh cell, $A_b = \pi(D/2)^2/N_c$. A similar approach was employed by Hopkins and Fauci [26] to simulate a suspension of microbial cells that they treated as point particles.

3 Approximate formulas for settling velocity

In this section, we review some of the existing analytical and experimental results on settling of a single particle under the action of gravity, starting with a brief derivation of the classical Stokes' law for a spherical particle in an unbounded fluid medium in 3D [43]. We will then modify Stokes' result for a circular particle in 2D, which corresponds to an idealized "infinite cylinder" in 3D. The case of a circular particle falling in a bounded fluid domain between two vertical walls is handled by introducing a "wall-correction factor" that is obtained using either experimental fitting or approximate analytical techniques. We report on the most commonly-used wall-correction factors, which are extensively reviewed by Champmartin and Ambari [11].

3.1 Stokes' law for a spherical particle in 3D

Two main forces act upon a massive particle settling while in a fluid: the gravitational force F_g, and the drag force F_d due to "friction" between the particle and the fluid. A particle that is initially at rest will accelerate under gravity, and as the particle begins to move through the fluid it experiences a drag force in the direction opposite to its motion that increases with the speed of the particle relative to the fluid. Once the drag force grows to equal the gravitational force, the two forces are in balance and no further acceleration occurs. The particle velocity in this equilibrium state is known as the settling or terminal velocity.

https://doi.org/10.4208/cicp.061113.050115a Published online by Cambridge University Press

Taking a sphere of diameter D and density ρ_s whose added mass relative to the fluid is $\frac{4}{3}\pi\left(\frac{D}{2}\right)^3(\rho_s-\rho_f)$, the net gravitational force acting on the sphere is

$$F_g=\frac{4\pi}{3}\left(\frac{D}{2}\right)^3 g(\rho_s-\rho_f). \tag{3.1}$$

The corresponding drag force is

$$F_d=\frac{1}{2}C_d\rho_f V^2\pi\left(\frac{D}{2}\right)^2, \tag{3.2}$$

where C_d is the drag coefficient and V is the velocity of the sphere relative to the fluid. The settling velocity V_s corresponds to the steady state in which drag and gravity forces are in balance, or $F_d=F_g$, so that

$$V_s=\sqrt{\frac{4gD(\rho_s-\rho_f)}{3C_d\rho_f}}, \tag{3.3}$$

keeping in mind that the drag coefficient on the right hand side also typically depends on the settling velocity, V_s. Indeed, at low values of particle Reynolds number, $Re=\rho_f DV_s/\mu$, the drag coefficient for a sphere is approximated by [3]

$$C_d=\frac{24}{Re}=\frac{24\mu}{\rho_f V_s D}. \tag{3.4}$$

Substituting this expression into (3.3) and solving for V_s we obtain Stokes' law

$$V_s=\frac{gD^2(\rho_s-\rho_f)}{18\mu}, \tag{3.5}$$

which is valid for $Re\lessapprox 0.1$.

3.2 Settling velocity for a circular particle in 2D

A similar argument may be used to derive the corresponding settling velocity for a circular particle in 2D. By considering a cylinder with diameter D and length ℓ, and then taking the limit as $\ell\to\infty$, we obtain a result that is relevant to our 2D geometry. The immersed cylinder has an added mass (relative to the fluid) of $m=\pi\left(\frac{D}{2}\right)^2\ell(\rho_s-\rho_f)$ for which the net gravitational and drag forces are

$$\widetilde{F}_g=\frac{\pi}{4}g\ell D^2(\rho_s-\rho_f), \tag{3.6}$$

$$\widetilde{F}_d=\frac{1}{2}\widetilde{C}_d\rho_f\widetilde{V}^2D\ell. \tag{3.7}$$

https://doi.org/10.4208/cicp.061113.050115a Published online by Cambridge University Press

Notice that the cross-sectional area factor $\pi(D/2)^2$ for the sphere in (3.2) is replaced by $D\ell$ for the cylinder, and the tildes are used here to distinguish the cylindrical quantities. We also make use of the drag coefficient for a cylinder from [3]

$$\widetilde{C}_d = \frac{8\pi}{Re\ln\left(\frac{7.4}{Re}\right)}, \tag{3.8}$$

which holds when $Re \ll 1$. The cylinder settling velocity is then obtained by equating the two forces in (3.6) and (3.7), which yields

$$\widetilde{V}_s = \sqrt{\frac{\pi g D(\rho_s - \rho_f)}{2\widetilde{C}_d \rho_f}}. \tag{3.9}$$

Observe that the cancellation of the length factor ℓ in computing this expression means that the same formula holds for the 2D geometry in the $\ell \to \infty$ limit. Furthermore, we observe that this expression is the same as that for the sphere in (3.3) except that the factor $\sqrt{4/3}$ is replaced here with $\sqrt{\pi/2}$, and of course the cylinder drag coefficient is also different.

When Eqs. (3.8)-(3.9) are taken together, they reduce to a single nonlinear equation for Re

$$f(Re) = Re - \frac{\rho_f g D^3(\rho_s - \rho_f)}{16\mu^2}\ln\left(\frac{7.4}{Re}\right) = 0, \tag{3.10}$$

which can alternately be written as an equation for $\widetilde{V}_s$. It is easy to show that the function $f(Re)$ is continuous on the interval $0 < Re < \infty$ and has the following properties:

$$\lim_{Re\to 0^+} f(Re) = -\infty, \quad \lim_{Re\to\infty} f(Re) = +\infty \quad \text{and} \quad f'(Re) > 0.$$

Therefore, the intermediate value theorem guarantees a unique positive real root for f. Newton's method may be used to solve (3.10) for Re, and we find that any initial guess for Re suffices since the convergence is so rapid. Table 1 lists values of $\widetilde{V}_s$ from (3.10) for parameters $D = 0.018$ and ρ_s ranging from 1.01 to 1.05. As expected, the settling velocity increases with particle density as in the Stokes case.

Table 1: Settling velocity $\widetilde{V}_s$ obtained from (3.10) with $\rho_f = 1$ and $D = 0.018$.

ρ_s	$\Delta\rho$	$\widetilde{V}_s$
1.01	0.01	0.0024
1.02	0.02	0.0045
1.03	0.03	0.0066
1.04	0.04	0.0086
1.05	0.05	0.0105

https://doi.org/10.4208/cicp.061113.050115a Published online by Cambridge University Press

3.3 Wall-corrected settling velocities

We now summarize a few of the most common formulas used to approximate the settling velocity of a particle in falling within a channel of width W bounded by two parallel, vertical walls. It is well-known that the bounding walls exert a retarding effect on a sedimenting particle [4,13,17,24,39,45,50] in that the settling velocity is lower in a channel than in an unbounded domain under the same conditions. The effect of wall interactions may be approximated using "wall correction factor" λ, that is expressed in the form [4]

$$\lambda(k,Re) = \frac{\widetilde{\mathcal{F}}_d(k)}{\mu V_c}, \tag{3.11}$$

where $\widetilde{\mathcal{F}}_d(k)$ is a drag force per unit length, V_c is the terminal settling velocity in the channel, and $k = D/W$ is the dimensionless particle size with $0 < k < 1$.

Note that the factor $\lambda(k,Re)$ depends on both Reynolds number and particle size; however, it is well known [13] that at either very low or very high values of Re, λ is nearly independent of Reynolds number. In this study, we are concerned with the low Re regime and so it is reasonable to assume that λ depends on k only. Below we summarize some of the more common wall correction factors that have been derived in the literature (see [4] for example), all of which have the same channel geometry as pictured in Fig. 2:

- White [50]: carried out experiments with wires and ebonite rods in a channel containing viscous liquids such as glycerin and paraffin. He obtained the following experimental fit for the drag force on a cylinder

$$\lambda(k) = \frac{-6.4}{\ln(k)}, \tag{3.12}$$

  whose domain of validity is restricted to $0 < k < 0.2$.

- Faxén [17, 24]: derived an approximate analytical solution of Stokes' equations, from which he obtained

$$\lambda(k) = \frac{-4\pi}{0.9157 + \ln(k) - 1.724k^2 + 1.730k^4 - 2.406k^6 + 4.591k^8}. \tag{3.13}$$

  Some authors claim that this approximation is valid for k as large as 0.5 [4], while others cite an upper bound of $k = 0.3$ or even lower [39], which is more in line with our numerical simulations (see Fig. 9 in Section 4).

- Takaisi [45]: solved Oseen's equations to obtain the approximation

$$\lambda(k) = \frac{-4\pi}{0.9156 + \ln(k)}, \tag{3.14}$$

  which is restricted to $0 < k < 0.2$. He also compared his formula to White's and showed that the two expressions match well when $k < 0.05$.

https://doi.org/10.4208/cicp.061113.050115a Published online by Cambridge University Press

If we now consider $\lambda(k)$ to be a known function of dimensionless particle size k, then Eq. (3.11) can be solved for the drag force per unit length as $\widetilde{\mathcal{F}}_d(k) = V_c \mu \lambda(k)$. Equating this expression with the gravitational force per unit length, $\widetilde{\mathcal{F}}_g = \frac{\pi}{4} g D^2 (\rho_s - \rho_f)$, we find the following formula for the confined (or wall-corrected) terminal settling velocity of a cylinder

$$V_c = \frac{\pi g D^2 (\rho_s - \rho_f)}{4\mu\lambda(k)}. \tag{3.15}$$

In the next section, this expression will be compared with numerically simulated values for the three choices of $\lambda(k)$ listed above.

4 Numerical results: Single particle case

In this section, we consider a single particle in two initial configurations: one a symmetric case with the particle released along the centerline, and the other an asymmetric case where the particle is released from an off-center location. We restrict ourselves to low values of Reynolds number, $Re \lessapprox 7$, where Re refers to a "final" Reynolds number based on the terminal settling velocity. Unless otherwise indicated, we choose physical parameters $\rho_f = 1$, $\rho_s = 1.01$ and $D = 0.08$. The wall and particle IB spring stiffness values are taken large enough that the walls and particle boundary do not deform "too much" from their initial shapes — taking $\sigma_w = \sigma_c = 3 \times 10^4$ keeps the relative error in these boundary shapes to within approximately 0.2%.

Except for the convergence study in Section 4.1, simulations are performed using the same grid spacing $h_x = h_y = 0.0083$ and time step $\Delta t = 10^{-5}$. We also select the number of IB points for the two channel walls (N_w) such that the ratio of spacing between wall points to fluid grid size is $h_w / \min(h_x, h_y) \approx \frac{1}{3}$, which is well within the factor of $\frac{1}{2}$ that is recommended to avoid leakage of fluid between IB points [37]. We also adjust the number of IB points for the particle (N_c) until the initial mesh computed by DistMesh satisfies the same criterion.

4.1 Convergence study

We begin by performing a convergence study that validates the first-order spatial accuracy of the IB algorithm discussed earlier in Section 2.2. For this purpose, we take a square domain with side length $L_x = L_y = 1$ containing a single particle released on the centerline. A sequence of four simulations is performed corresponding to fluid grids with $N_x = N_y = 56$, 112, 224 and 448 points, and the settling velocity V_s is used as a representative measure of the solution accuracy. The difference between values of V_s on successive grids is calculated and the results are plotted in Fig. 4, which demonstrates that our numerical solution converges in V_s as the grid spacing is reduced. The curve is nearly a straight line on the log-log scale, and the slope of 0.85 obtained from a least squares fit

https://doi.org/10.4208/cicp.061113.050115a Published online by Cambridge University Press

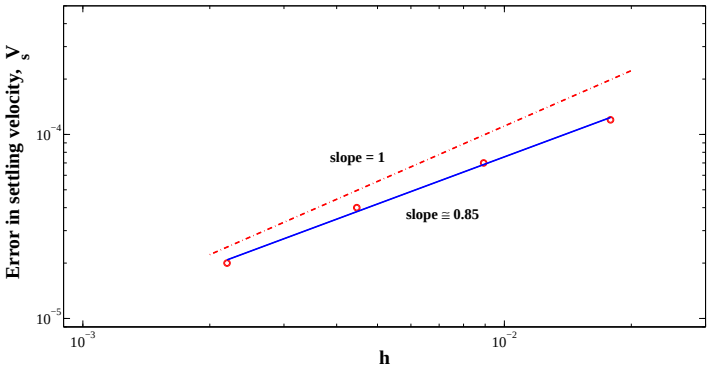


Figure 4: Convergence study in the settling velocity V_S for a single particle released along the centerline. The difference in V_S on successively finer grids is plotted versus grid spacing h. The solid straight line (with slope 0.85) corresponds to a linear least squares fit to the computed points.

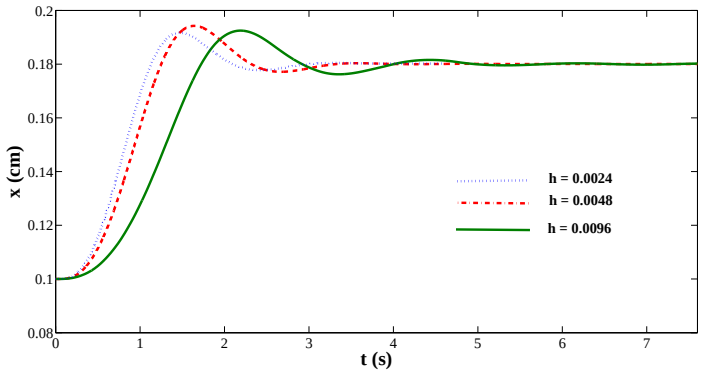


Figure 5: Long-term simulation of a single particle released off-center, showing the horizontal location as the grid spacing is reduced.

suggests that our implementation of the IB method is close to the expected first-order accuracy. Similar convergence rates are observed for other quantities such as fluid velocity, IB position, etc.

In this paper, our primary interest is in simulating particles with more complicated settling dynamics that take place over much longer time intervals, for which even small errors in quantities like V_S will accumulate. As an illustration of this accumulation of errors over longer times, we also simulate an off-center particle that exhibits more interesting dynamics wherein the particle approaches the terminal settling velocity while simultaneously oscillating back and forth horizontally around the channel centerline (further discussion of the dynamics is given in Section 4.4). In Fig. 5 we provide a plot of the horizontal location of the particle versus time for a choice of three different grid spacings. In all cases, the particle eventually settles down to a position along the channel center-

https://doi.org/10.4208/cicp.061113.050115a Published online by Cambridge University Press

line $x = 0.36$, and while the solutions are also seen to converge in h, the effect of error accumulation over intermediate times is clearly evident. As a result, we focus on direct comparisons using global quantities such as terminal settling velocity and drag coefficient, which are supplemented by qualitative comparisons of the particle dynamics for long-time simulations.

4.2 Comparison with Stokes' law

We aim next to validate the numerical method using the settling velocity $\widetilde{V}_s$ for a cylinder in an unbounded medium. However, we recall that our doubly periodic geometry implies that a single particle actually corresponds to an infinite array of sedimenting particles. Therefore, in the absence of solid boundaries or any other mechanism for dissipating energy, the net effect of gravity acting on such an infinite array of mass-bearing particles will be to accelerate the particles and the surrounding fluid indefinitely. This situation is clearly non-physical, and so instead we introduce walls into the domain that are located "far enough" from the particle so as to minimize wall-particle interactions and yet still permit the particle to reach its natural terminal velocity. To this end, we take a fluid domain with side lengths $L_x = L_y = L$, particle diameter $D = 0.018$ cm, introduce two vertical walls separated by a distance $W = L - 0.04$, and perform a sequence of computations with successively larger L varying between 1 and 7 cm. The fluid viscosity here and in the next section is $\mu = 1$ g/cms, which we remark is much larger than in later sections because a meaningful comparison to $\widetilde{V}_s$ is only possible at low Reynolds number.

The computed values of settling velocity are summarized in Table 2, from which we observe that as L increases, V approaches a limiting value of roughly 0.001674 cm/s. The results have clearly converged for the largest domain size, but the limiting value of V is significantly less than the Stokes settling velocity from Eq. (3.9), $\widetilde{V}_s = 0.00239$ cm/s. We suspect that this discrepancy is due to a combination of effects arising from grid resolution, first-order dispersive errors in our numerical scheme, and the increase in the effective thickness of the walls and particle owing to the delta function smoothing width (this last effect is discussed further in Section 4.3.2).

Table 2: Computed settling velocity as a function of domain size L for $D = 0.018$.

L	computed V
1	0.001230
2	0.001462
3	0.001565
4	0.001635
5	0.001673
6	0.001674
7	0.001674

https://doi.org/10.4208/cicp.061113.050115a Published online by Cambridge University Press

4.3 Single particle released along the centerline

We next consider the domain pictured in Fig. 2 wherein the particle is released along the center of the channel. Symmetry suggests that any forces generated by particle-wall interactions are balanced and so the particle should fall along the centerline without veering to either side. We perform a number of parametric studies that investigate the effect of changes in fluid domain size $[0,L_x]\times[0,L_y]$, density difference $\Delta\rho$, and relative particle size k on the settling velocity. As in the previous section, simulations are restricted to low Reynolds number by taking $\mu=1$.

4.3.1 Dependence of settling velocity on density difference $\Delta\rho$

For a fixed channel size with $W=0.98$ and $L_x=1$, we vary $\Delta\rho$ between 0.01 and 0.17. Fig. 6 shows that the wall-corrected settling velocity V_c increases linearly with $\Delta\rho$, which is consistent with Eq. (3.15). We also investigate the effect of increasing the channel length by taking $L_y\in\{3,10,16\}$, and observe that the influence of periodic copies in the y–direction is greatest for the shortest channel ($L_y=3$) which also yields the largest settling velocity. As the channel length is increased, the settling velocity decreases until by $L_y=16$ the results appear to have converged and are closest to Faxén's formula (3.13).

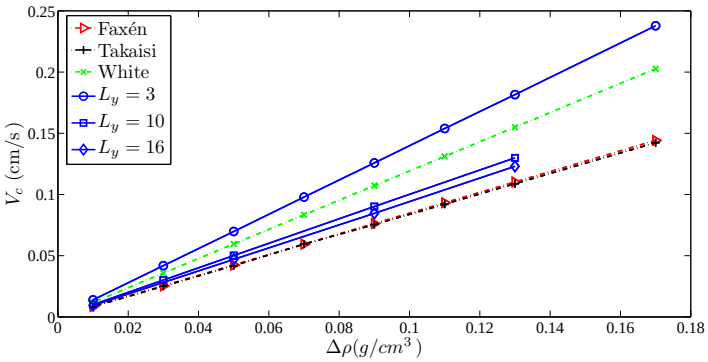


Figure 6: Settling velocity as a function of $\Delta\rho$. Parameter values: $L_x=1, L_y\in\{3,10,16\}, D=0.1, W=0.98, k=0.102$.

4.3.2 Dependence of settling velocity on particle size k

As mentioned in Section 3.3, the work of Faxén, White, Takaisi and others suggests that λ depends only on k at low Re which motivates this next study of the effect of dimensionless particle size. We again fix the channel width $W=L_x-0.04$, and then vary k by choosing values of particle diameter $D\in[0.018,0.96]$. Alongside the computed results in Fig. 7, we have displayed corresponding estimates of the confined settling velocity V_c calculated from Eq. (3.15) with the three wall correction factors (3.12)-(3.14). The unbounded cylindrical settling velocity $\widetilde{V}_s$ is also shown for comparison purposes, which

https://doi.org/10.4208/cicp.061113.050115a Published online by Cambridge University Press

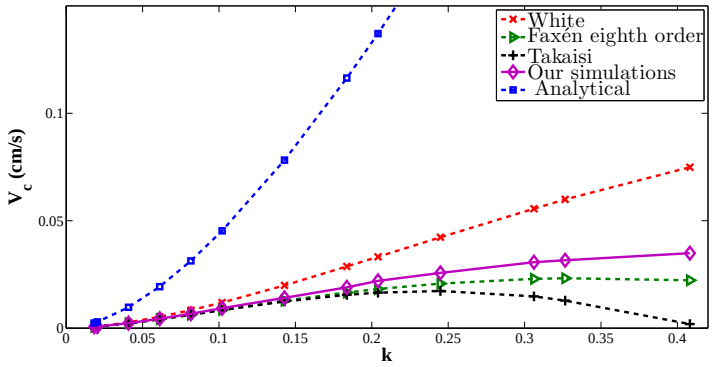


Figure 7: Variation of settling velocity with k for computations and various analytical expressions. Parameter values: $L_x=1$, $L_y=16$, $\mu=1$.

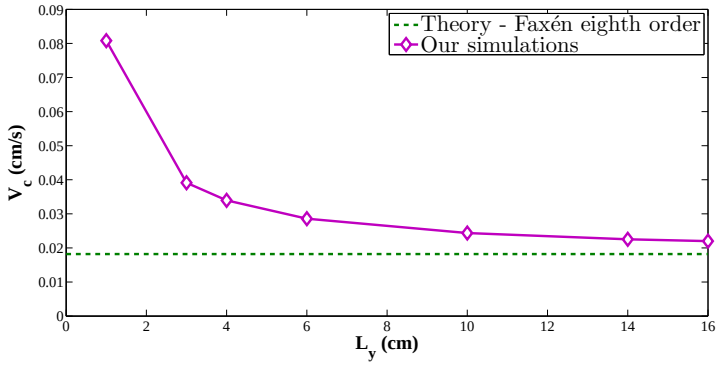


Figure 8: Effect of increasing the channel length L_y and hence reducing the impact of the periodic copies in y. Parameter values: $\mu=1$, $L_x=1$, $D=0.2$, $W=0.98$, $k=0.2041$.

clearly diverges from the wall-corrected values away from $k=0$. For these simulations, Re was in the range $[1.2\times10^{-5},1.8\times10^{-2}]$.

Our computed results match most closely with Faxén's formula, which is often cited as the most accurate approximation for wall-corrected settling velocity. We also studied the effect of changes in the channel length L_y in order to determine whether there is any interference between vertical periodic copies of the particle due to the periodicity assumption. Results for $L_y\in[1,16]$ are displayed in Fig. 8 which clearly show that our computed settling velocity converges to Faxén's prediction when $k\lessapprox0.2$.

On the other hand, there remain significant deviations between Faxén's results and our computations for $k>0.2$ as demonstrated in Fig. 9. Faxén's settling velocity levels out and attains a maximum near $k=0.3$, after which it falls to zero near $k=0.6$. In contrast, our computed results attain a maximum that is roughly 60% larger ($V_c\approx0.035$) and plateaus for values of k in the range $[0.4,0.8]$.

Our computed settling velocity drops to zero when k approaches 1, which is clearly

https://doi.org/10.4208/cicp.061113.050115a Published online by Cambridge University Press

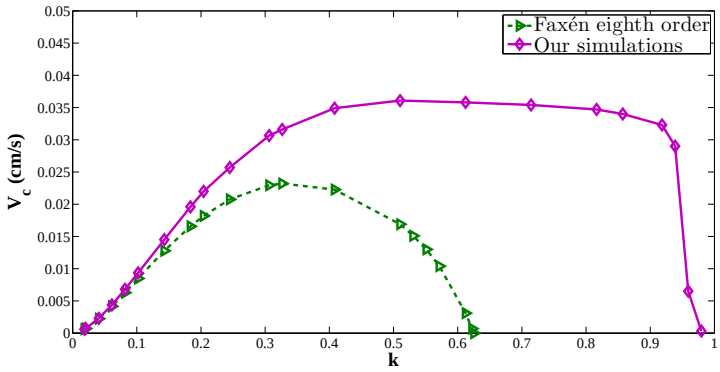


Figure 9: Settling velocity versus k, comparing our simulations to Faxén's approximation. Parameter values: $L_x=1$, $L_y=16$, $\mu=0.01$.

justified since the particle must slow to a stop as it comes into direct contact with the stationary walls. However, our results in Fig. 9 show that V_c actually tends to zero not at $k=1$ but rather $k\approx 0.96$. This apparent reduction of 0.04 in the channel width is due to the approximate delta function which introduces an extra "effective thickness" to both the walls and the particle. Indeed, the numerical simulations in [42] show that for the cosine delta function, the effective IB thickness is approximately $1.6h$[†]. Consequently, a particle of diameter D should have an effective diameter of $D_{eff}\approx D+3.2h$, and each wall should extend an additional distance of $3.2h$ into the channel. Taken together this suggests a total reduction of $6.4h$ in the effective channel width or approximately 0.053, which is quite close to our observed reduction of 0.04.

The behavior of our numerical simulations can be summarized as follows:

- For small particle diameters corresponding to $k\in[0,0.2]$, the particle is far enough from the channel walls that the effect of wall drag is not significant. In this range, the dependence of the settling velocity is also roughly proportional to k, which is consistent with Faxén's result.
- For intermediate values of k in the range $[0.4,0.8]$, the settling velocity is at a maximum and remains approximately constant with k. For these particle sizes, particle-wall interactions are at long range and are mediated by the fluid.
- For values of $k\in[0.8,1.0]$, the particle is very close to the walls and experiences close-range interactions that slow the particle significantly.

Of course, we must keep in mind that the validity of Faxén's approximation is limited to $k\lessapprox 0.2$ and so it is no surprise that our results differ so much for larger k.

[†]Note that the effective thickness depends on the choice of regularized delta function. Bringley [9] computed an effective thickness closer to $1.25h$ for a different but closely-related approximate delta function.

https://doi.org/10.4208/cicp.061113.050115a Published online by Cambridge University Press

4.4 Single particle released off-center

We next consider the asymmetric initial condition shown in Fig. 10 where a particle of diameter $D = 0.08$ cm is released from a distance $W/2$ to the left of center and for which the resulting dynamics are more interesting. We consider two different channel widths $W = 4D$ and $8D$, channel length $L_y = 3$, and vary the Reynolds number by taking values of viscosity $\mu \in [0.006, 0.018]$ g/cms. This choice of parameters permits us to draw direct comparisons with the analytical and experimental results reported by Sucker and Brauer [44], as well as the numerical simulations of Feng et al. [18].

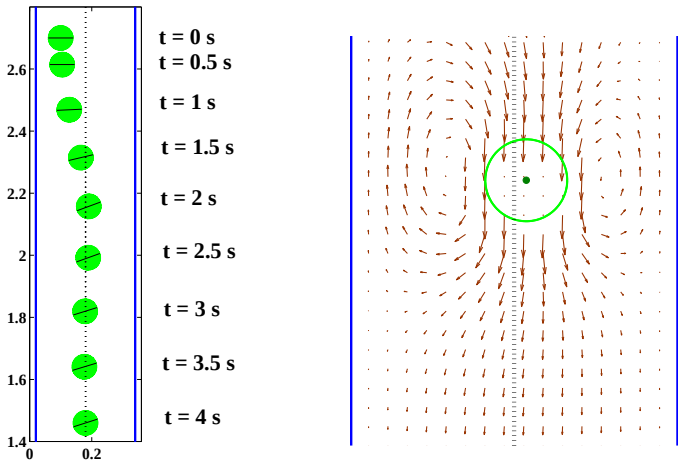


Figure 10: (Left) Settling dynamics for a single particle released off-center, with channel width $W = 4D$ and $Re = 4.9$. The solid line through the center of the particle highlights the rotational motion. (Right) Velocity vector plot at time $t \approx 2$ s.

The settling dynamics are pictured in Fig. 10 for parameter choices $W = 4D$ and $Re = 4.9$. As the particle begins to fall, it drifts toward the channel centerline, ultimately attaining its terminal settling velocity there. The particle trajectories depicted in Fig. 11 show that the particle actually overshoots the centerline and then undergoes a damped oscillation about the channel midpoint. Simulations for three other values of $Re = 2.2$, 3.7 and 4.4 are also displayed in Fig. 11, which demonstrates that the magnitude of these oscillations increases with Re. These dynamics are similar to a simple damped harmonic oscillator with damping coefficient proportional to Re^{-1}.

The particle also undergoes a small-amplitude rotational motion as it falls through the channel, which is easily visualized by following the progress of the straight line segment drawn through the interior of the particle in Fig. 10. Another view of the rotational dynamics is provided by the plots of angular velocity in Fig. 12 for the same $Re = 4.9$ simulation.

As the particle drifts from its starting location toward the centerline, it experiences a slight counter-clockwise rotation which slows at it approaches its terminal velocity along

https://doi.org/10.4208/cicp.061113.050115a Published online by Cambridge University Press

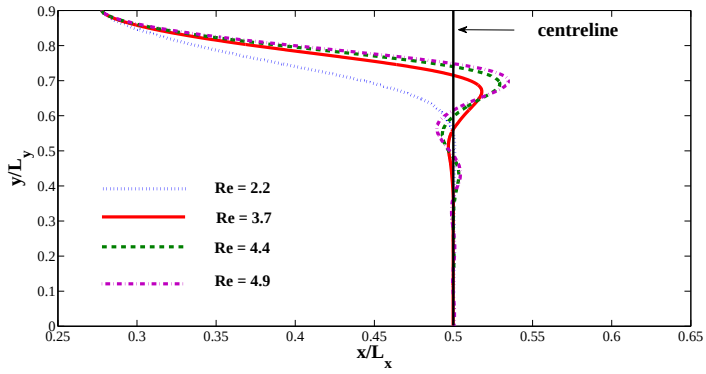
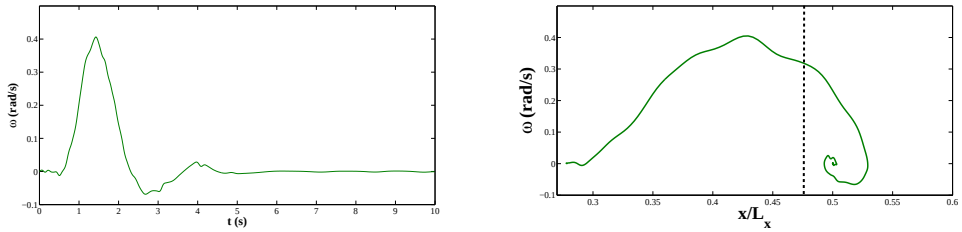


Figure 11: Settling trajectories for an off-center particle at different Reynolds number, with channel width $W=4D$.



(a) (b)

Figure 12: Angular velocity for a single particle released off-center, with $W=4D$ and $Re=4.9$. Positive ω corresponds to counter-clockwise rotation. (a) Variation of angular velocity with time. (b) Angular velocity versus horizontal location, where the dashed line represents the channel centerline.

the centerline, leaving the particle with an orientation slightly tilted relative to its initial state.

Simulations were also performed on a channel with twice the width ($W=8D$) for four different values of $Re=1.5$, 2.4, 4.2, and 6.4. The resulting particle trajectories are shown in Fig. 13 where we observe no overshoot of the centerline, which is in contrast with the $W=4D$ results in Fig. 11. We attribute this behavior to the fact that in a wider channel the wall-particle interactions that drive the horizontal motions are substantially weaker. Correspondingly, the angular velocity of the particle is an order of magnitude smaller than the $W=4D$ case, and so it is not shown here.

We conclude our discussion of the single-particle case by comparing values of the drag coefficients based on the cylinder drag formula $\widetilde{C}_d=\pi(\rho_s-\rho_f)gD/(2\rho_f V_c^2)$ derived from Eq. (3.9). The results are summarized in Fig. 14 along with values taken from the following two papers:

- Feng, Hu and Joseph [18], who performed finite element simulations of a single particle settling in channels of width $4D$ and $8D$. We will denote their work using the abbreviation FHJ since it is referred to often in the rest of this paper.

https://doi.org/10.4208/cicp.061113.050115a Published online by Cambridge University Press

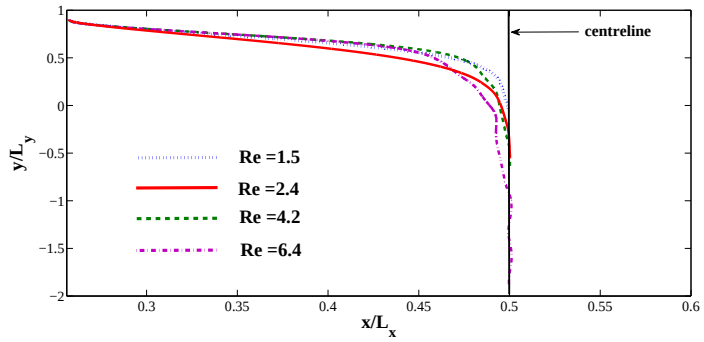


Figure 13: Settling trajectories for an off-center particle at different Reynolds number, with channel width $W=8D$.

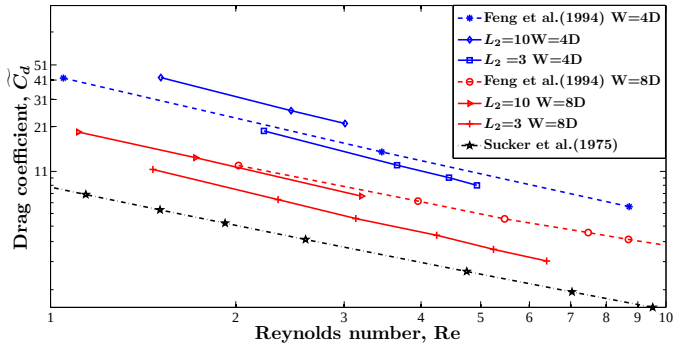


Figure 14: Comparison of drag coefficients for a single particle settling in channels of width $4D$ and $8D$. Experimental results of Sucker and Brauer [44] and numerical results of FHJ [18] are included for comparison purposes (reproduced with permission). Parameter values for our simulations: $D=0.08$, $L_y=3$, $L_x=0.36$ (when $W=4D$) and $L_x=0.68$ (when $W=8D$).

- Sucker and Brauer [44], who developed an empirical formula by fitting to experimental data on a cylinder settling in a very large fluid domain. They also developed an approximate analytical formula for an unbounded domain that matched closely with their experimental data.

Our simulations match reasonably well with those of FHJ, particularly for the $W=8D$ channel in the large L_y limit. Sucker and Brauer's empirical formula clearly deviates from both ours and FHJ's results because it strictly applies only to unbounded domains. While these results are encouraging, a much more comprehensive comparison is required before we can draw any solid conclusions about the accuracy of our numerical approach.

5 Numerical results: Two particle case

The remainder of our simulations are based on two circular particles with identical diameter D that settle in a channel of length $L_y=3$. The particle dynamics are driven by

https://doi.org/10.4208/cicp.061113.050115a Published online by Cambridge University Press

a combination the wall interactions observed in the previous section along with particle-particle interactions.

One of the main aims in this section is to reproduce the well-known phenomenon in suspension flows wherein pairs of particles interact and undergo a "drafting, kissing and tumbling" behavior (which we abbreviate by DKT). This phenomenon has been established experimentally [19,29] and demonstrated numerically in [18], and can be justified physically as follows. The leading particle creates in its wake a reduction in pressure as it falls, and provided that the trailing particle is close enough to interact with the wake it experiences a smaller drag force than the leading particle. As a result the trailing particle speeds up and the two particles approach each other — this initiates the "drafting phase". As the particles get closer they nearly touch or "kiss" after which the kissing particles momentarily form a single longer body that is aligned parallel with the flow. This parallel arrangement is unstable and the particles subsequently tumble and swap leading/trailing positions — this is the "tumbling phase". After tumbling the particles separate and one of two things occurs: either the DKT process repeats, or else the particles separate until the interaction force becomes so weak that they fall independently at their own "natural" wall-corrected vertical settling velocity.

In the simulations to follow, we use four different initial configurations of the particles as depicted in Fig. 15:

(a) Aligned vertically, one above the other along the channel centerline.

(b) Aligned vertically, but shifted to the left to a position midway between the channel centerline and the left wall.

(c) Aligned horizontally, and placed symmetrically about the centerline.

(d) Aligned horizontally, but shifted to the left of center.

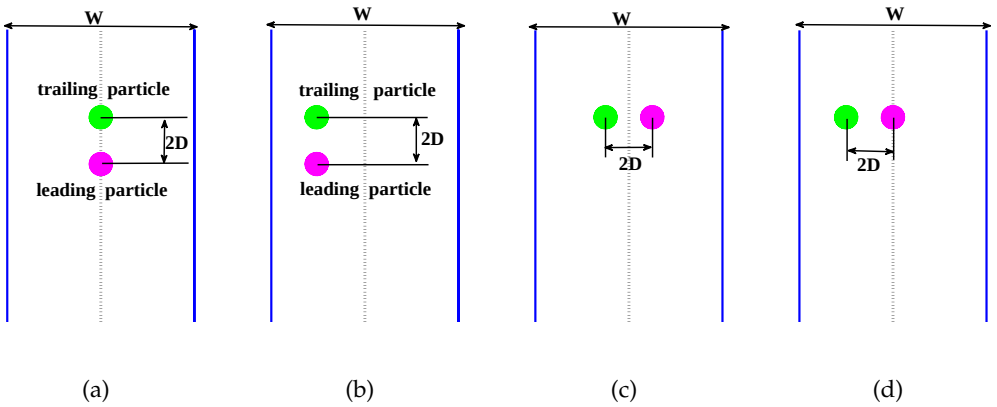


Figure 15: Four initial configurations of the two-particle settling problem, with particle centers separated by distance $2D$: (a) aligned vertically, along the channel centerline; (b) aligned vertically, offset to the left of center; (c) aligned horizontally, symmetric about the centerline; (d) aligned horizontally, offset to the left of center.

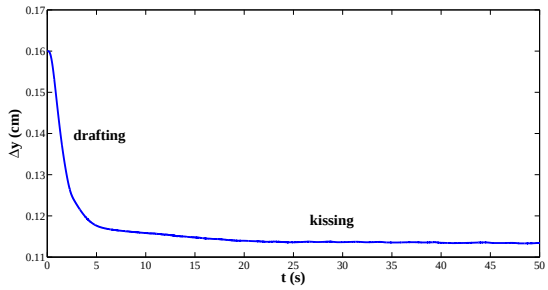
https://doi.org/10.4208/cicp.061113.050115a Published online by Cambridge University Press

In all cases, the particle diameter is $D = 0.08$ cm and the initial separation distance between the centers of mass of the two particles is $2D$. As in the previous section, we also consider two channel widths, $W = 4D$ and $W = 8D$, and compare solutions for various Reynolds numbers by varying viscosity over the range $\mu \in [0.0015, 0.16]$.

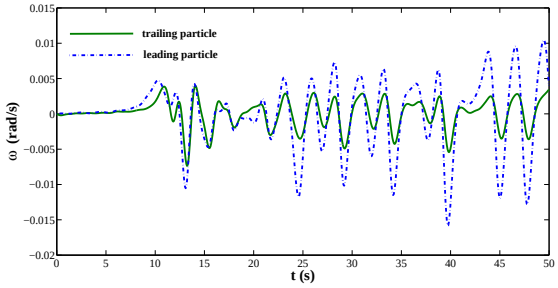
5.1 Two vertically-aligned particles, released on the centerline

Consider the initial configuration shown in Fig. 15(a) where two particles are released on the channel centerline with their centers separated by a vertical distance of $2D$. We perform simulations using channel width $W = 8D$ and three different Reynolds numbers, $Re = 3$, 14 and 80.

Starting with the smallest value of $Re = 3$, we observe that both particles remain along the channel centerline throughout the simulation, and while drafting and kissing behavior is observed, no tumbling occurs. As can be seen in Fig. 16(a), the trailing particle approaches the leading particle, coming quite close but never touching each other (owing to the increase in effective particle diameter from the delta function, discussed at the end of Section 4.3.2). After kissing, the particles fall as a single body with no noticeable relative motion. The angular velocity plot in Fig. 16(b) indicates that there is a very small-amplitude oscillation in orientation angle (not visible to the naked eye), which we



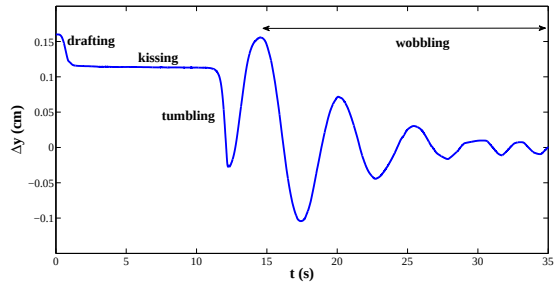
(a) Vertical separation distance



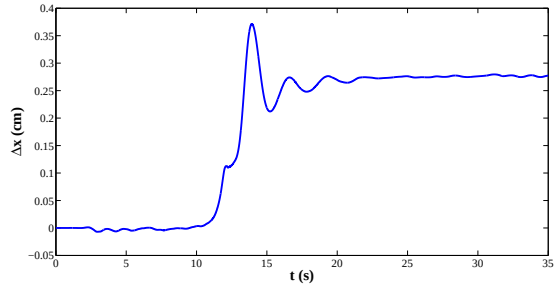
(b) Angular velocities

Figure 16: Settling dynamics of two particles initially aligned vertically, with parameters $W = 8D$ and $Re = 3$. (a) Vertical separation distance. (b) Angular velocity ω (positive = counter-clockwise rotation).

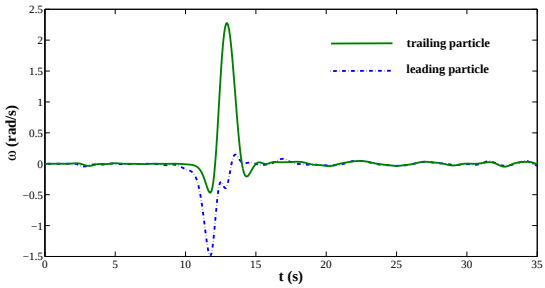
https://doi.org/10.4208/cicp.061113.050115a Published online by Cambridge University Press



(a) Vertical separation distance



(b) Horizontal separation distance



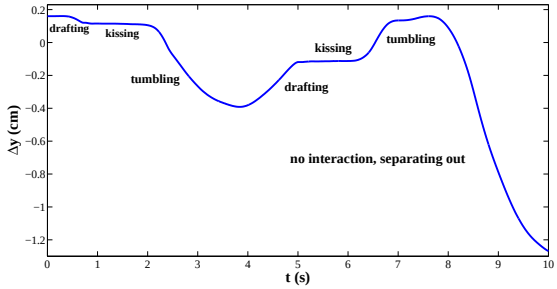
(c) Angular velocities

Figure 17: Settling dynamics of two particles at $Re=14$ initially aligned vertically along the centerline, with channel width $W=8D$. (a) Vertical separation distance. (b) Horizontal separation distance. (c) Angular velocity ω (positive = counter-clockwise).

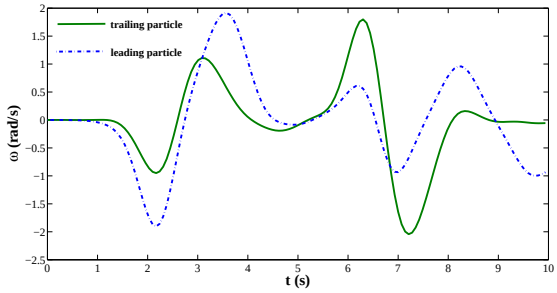
suspect is due to the oscillation of IB points arising from the IB spring forces maintaining the particle shape. These oscillations are an artifact of our IB approach that uses a stiff spring network to approximate a rigid particle, and have been well-documented in the immersed boundary literature [5, 8, 12].

When Reynolds number is increased to $Re=14$, the particle dynamics become more complex and give rise to a DKT cycle, with the trailing particle catching up with and passing the leading particle near time $t\approx 11$ s. The subsequently tumbling action is evident from Fig. 17(a) as the vertical separation distance becomes negative. After this initial

https://doi.org/10.4208/cicp.061113.050115a Published online by Cambridge University Press



(a) Vertical separation distance



(b) Angular velocities

Figure 18: Settling dynamics of two particles at $Re=80$ initially aligned vertically along the centerline, with channel width $W=8D$. (a) Vertical separation distance. (b) Angular velocity ω (positive = counter-clockwise).

tumble, the particles separate horizontally and drift to locations symmetrically opposite each other across the centerline, separated by a distance of roughly 0.27 cm. For the next 20 seconds, they maintain their horizontal distance but exchange leading/trailing positions via a periodic modulation of the vertical velocity with decaying amplitude. After time $t\approx 35$ s, the particles have essentially reached a steady state in which they are falling at constant velocity and maintaining a constant separation distance (refer to Fig. 17(b)).

The angular velocity plot in Fig. 17(c) shows that both particles experience a significant rotation during the tumbling phase that is several orders of magnitude larger than the small "wobbling" motion observed in the $Re=3$ case. In fact, the growth in rotational motion appears to be connected with the horizontal symmetry breaking that initiates tumbling motion, although by time $t=15$ s the rotational motion has also subsided.

As the Reynolds number is further increased to $Re=80$, we observe in Figs. 18 and 19 another qualitative change in solution behavior. The particles begin with a DKT exchange such as that observed at $Re=14$; however, in this case the two particles drift together toward the left channel wall instead of the channel centerline. Next, the particles reverse direction toward the right wall and undergo a second DKT exchange, after which the particle that was initially trailing ends up in the lead. These two DKT exchanges are accompanied by a back-and-forth rotation motion of each particle (refer to Fig. 18(b)),

https://doi.org/10.4208/cicp.061113.050115a Published online by Cambridge University Press

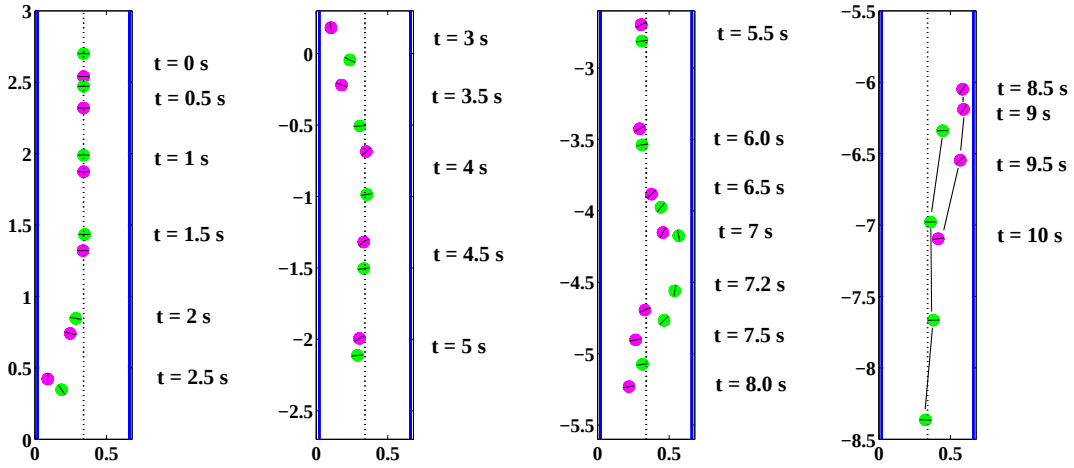


Figure 19: Snapshots of particle interactions in the channel of width $W=8D$ with $Re=80$, for the case when the particles are initially aligned vertically along the channel centerline.

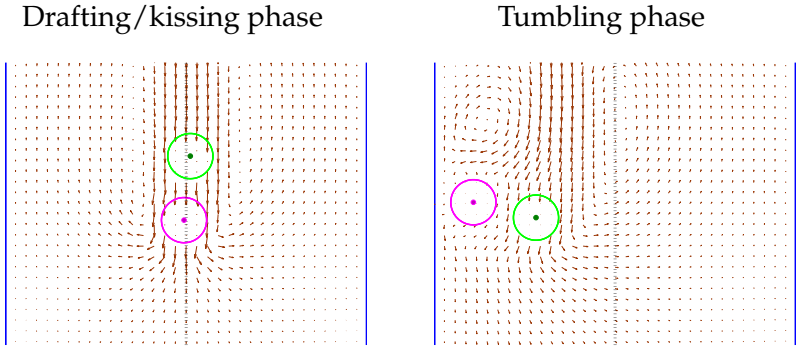


Figure 20: Velocity vector plots for the drafting/kissing (left) and tumbling phase (right) for the case when the particles are initially aligned vertically along the channel centerline. Parameters: $W=8D$ and $Re=80$.

and once again it appears to be growth in this small "wobble" that initiates tumbling. We also note that when a particle nears the left wall it experiences a clockwise rotation, while the rotation is reversed near the right wall — this behaviour is consistent with physical intuition, which suggests that wall drag arising at the channel wall should cause a rolling-type motion that slows the portion of the particle closest to the wall.

FHJ [18] performed a similar computation at $Re=70$ that exhibits results consistent with ours up to time $t\approx 5.4$ s. However, they terminate their computation at this point and there is no indication in their paper of the subsequent dynamics. Indeed, we find that after the second tumble, the particles separate vertically as they migrate toward the center of the channel so that by time $t=10$ s they settle at the same speed and no longer interact in any significant way. Our computations also exhibit much the same qualitative behavior as the experiments reported in [19,29] and numerical simulations from [21,46].

https://doi.org/10.4208/cicp.061113.050115a Published online by Cambridge University Press

5.2 Two vertically-aligned particles, released off-center

Next, consider the asymmetric initial configuration in Fig. 15(b) with two particles displaced to the left of center at location $x = W/4$ but still aligned vertically (and separated by a distance $2D$). For a channel of width $W = 4D$ and Reynolds numbers $Re = 1.5$, 2, 10, the behavior is summarized in Fig. 21. In all three cases, the particles start by drifting to the right, with the trailing particle approaching the centerline and the leading particle moving to a point roughly mid-way between the centerline and the right wall. At the same time, the trailing particle accelerates in the wake of the leading particle so that they approach the same height. After this initial realignment, the lowest Reynolds number cases ($Re = 1.5$, 2) undergo a further horizontal adjustment so that the two particles relocate to positions symmetric about the centerline; interestingly, for the $Re = 10$ case the sustain their asymmetric configuration. After that, the particles fall at roughly constant vertical speed and without changing their x-locations. The snapshots in Fig. 22 for the

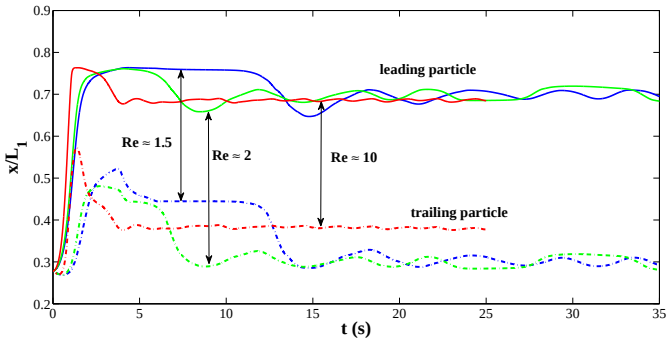


Figure 21: Horizontal particle locations for two particles initially aligned vertically but off-center. Parameter values: $W = 4D$ and $Re = 1.5$, 2, 10.

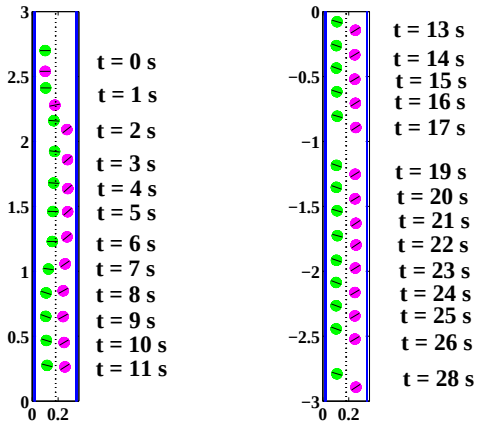


Figure 22: Snapshots of particle interactions for the case when the particles are initially aligned vertically, but off-center. Parameter values: $W = 4D$ and $Re = 2$.

https://doi.org/10.4208/cicp.061113.050115a Published online by Cambridge University Press

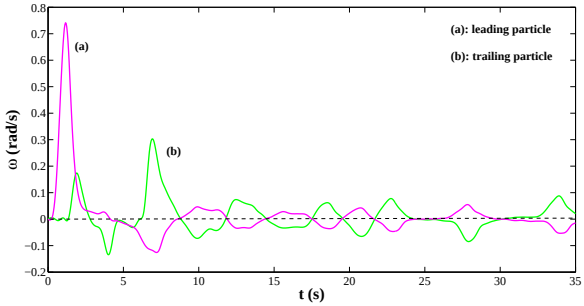
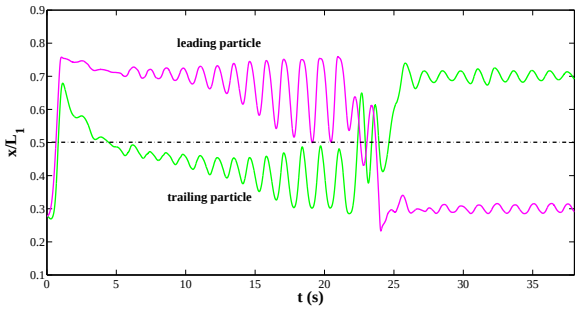
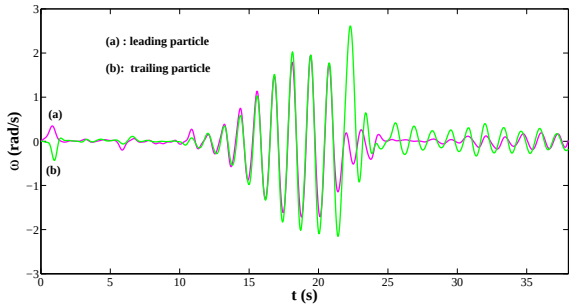


Figure 23: Angular velocity ω for two particles initially aligned vertically and off-center. Parameter values: $W=4D$ and $Re=2$.



(a) Horizontal positions



(b) Angular velocities

Figure 24: Settling dynamics of two particles initially aligned vertically and off-center, with parameters $W=4D$ and $Re=47$. (a) Horizontal positions. (b) Angular velocity ω (positive = counter-clockwise).

$Re=2$ illustrate these dynamics and also demonstrate that the particles do not enter either kissing or tumbling phases.

Both particles experience a synchronized rotational motion as shown in Fig. 23 for $Re=2$, although the angular velocity is not as large as was observed during the tumbling phase in the previous section. Corresponding results for channel width $W=8D$ do not exhibit any significant difference in qualitative behavior.

https://doi.org/10.4208/cicp.061113.050115a Published online by Cambridge University Press

For a higher value of Reynolds number $Re=47$, very different dynamics are observed in Figs. 24 and 25. Up to time $t\approx 7$s the dynamics are consistent with the lower Re cases as the particles migrate to the right with the leading particle approaching closest to the wall. However, at this point the particles separate horizontally and begin a back-and-forth oscillation that grows in amplitude between $t\approx 7$ and 21 s, until the oscillating particles overlap with each other near the centerline. Referring to the angular velocity plot in Fig. 24(b), the horizontal oscillations over this interval are accompanied by a synchronized rotation of both particles. Near $t\approx 21$ s, the particles undergo a strong interaction and move to opposite sides of the channel (still symmetrically placed about the centerline), which is essentially a steady state.

5.3 Two horizontally-aligned particles

We next simulate the motion of two particles released from same height in a channel of width $W=8D$ using the two different horizontal alignments depicted in Figs. 15(c) and (d) — the first in which the particles are placed symmetrically about the channel centerline, while the second has an asymmetric arrangement that is shifted to the left of center. Our primary aim here is to validate our results against the finite element computations of FHJ [18] for the specific case of $W=8D$ and $Re=1.52$. These authors simulated the particle dynamics pictured in Fig. 26, which can be separated into three distinct phases:

i. a first phase, consisting of a rapid re-adjustment up to time $t^*\approx 500$ (measured in dimensionless time units, with $t^*=t\sqrt{g/D}$) during which the particles separate horizontally to locations equally-spaced from the left and right walls;

ii. a second phase, where the particles maintain their symmetric horizontal positions and fall together at the same speed until $t^*\approx 4000$;

iii. a third phase, in which the particles drift to the right toward a new asymmetric equilibrium state where the left particle oscillates about the centerline, while the right particle oscillates with smaller amplitude about a point closer to the wall.

We remark that FHJ's simulations were intended to mimic the experiments of Jayaweera and Mason [28], who considered two long thin cylinders settling in a large tank at Reynolds numbers between 0.1 and 1.0. In Jayaweera and Mason's paper, they make mention of the first two phases but not phase iii.

We begin with the symmetric initial conditions where the particles are released from locations $x=\frac{L_x}{2}\pm\frac{W}{8}$ and Reynolds number $Re=1.6$, which is very close to FHJ's value. The horizontal locations of the simulated particles are pictured in Fig. 27, where we have rescaled the plot axes to use the same dimensionless variables in Fig. 26. The particles reach a steady state at positions $x/D\approx 2.25$ and 5.75, which are very close to those obtained in FHJ's phase ii. Furthermore, the phase i transient ends at roughly the same time of $t^*\approx 500$. We are therefore confident that our simulated particle dynamics are consistent with FHJ's results during phases i and ii.

https://doi.org/10.4208/cicp.061113.050115a Published online by Cambridge University Press

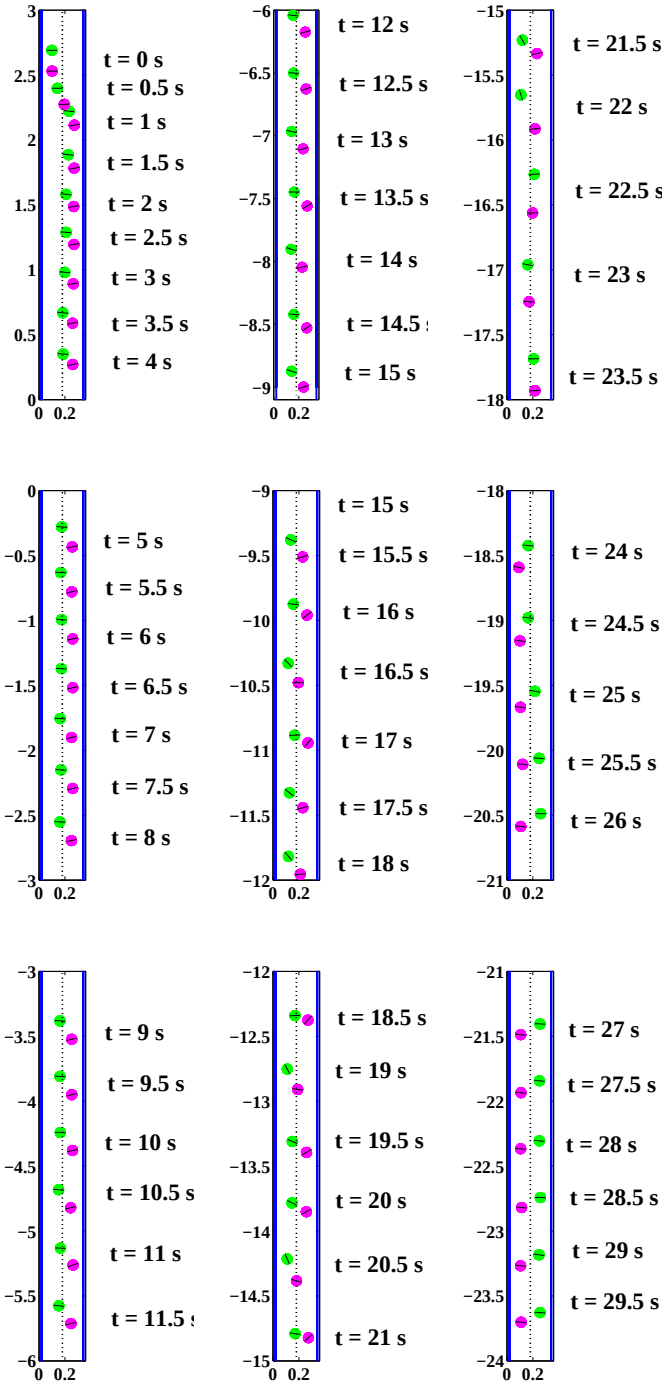


Figure 25: Snapshots of particle interactions for two particles initially aligned vertically, but off-center. Read from top to bottom, then left to right. Parameter values: $W = 4D$ and $Re = 47$.

https://doi.org/10.4208/cicp.061113.050115a Published online by Cambridge University Press

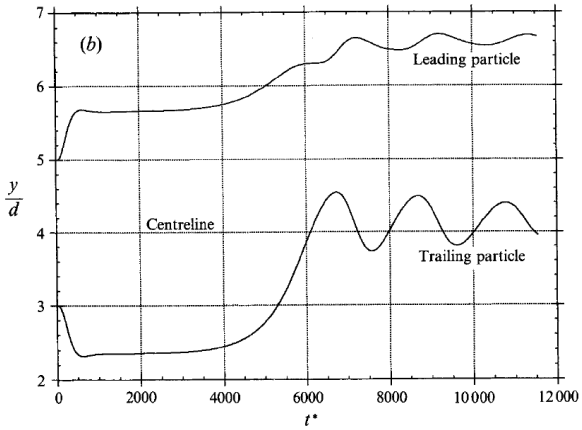


Figure 26: Horizontal locations of the two particles, as simulated by FHJ. Parameters: $W=8D$, $Re=1.52$. Reproduced from [18, Figure 32(b)], with permission.

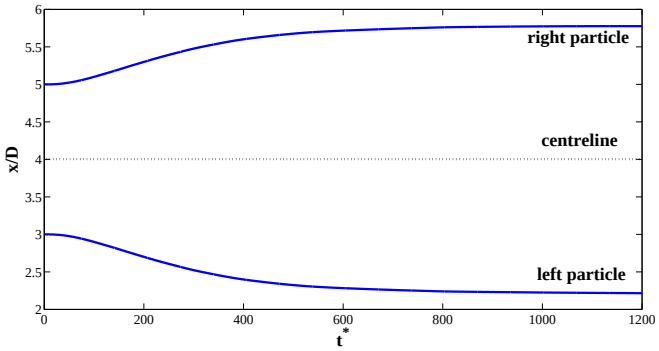


Figure 27: Horizontal positions for two particles released at the same height and positioned symmetrically about the centerline. Parameter values: $W=8D$ and $Re=1.6$.

However, we do not see any evidence of FHJ's phase iii behaviour since our simulated particles never leave their steady state configuration achieved in phase ii, even when t^* is taken much greater than 4000. Dynamics similar to FHJ's phase iii have been simulated by Aidun and Ding [1] using a lattice-Boltzmann method, and they ascribe this periodic behavior to the appearance of a solution bifurcation. It is likely that such a bifurcation is sensitive not only to parameter values but also to the presence of numerical error; therefore, it is possible that the first-order accuracy of our IB method could be preventing us from capturing this phase iii transition. Nonetheless, we did indicate earlier that Jayaweera and Mason [28] make no mention of phase iii dynamics in their experiments, and so the question of whether this phase iii transition is even physically reasonable remains open.

We repeated the previous calculation with a larger Reynolds number, $Re=4.4$, and the results in Figs. 28 and 29 exhibit similar dynamics to the lower Re case. These results

https://doi.org/10.4208/cicp.061113.050115a Published online by Cambridge University Press

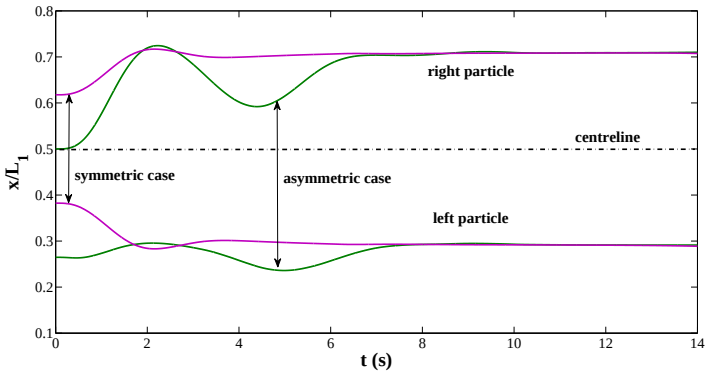


Figure 28: Horizontal particle positions for two particles initially located on the same horizontal line. Both symmetric and asymmetric initial conditions are pictured. Parameter values: $W=8D$ and $Re=4.4$.

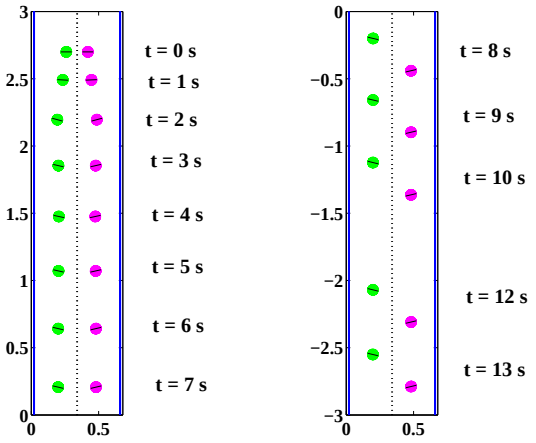


Figure 29: Snapshots of particle interactions for two particles initially aligned horizontally and centered. Parameter values: $W=8D$ and $Re=4.4$.

give us some confidence that our IB simulations are reproducing physically-relevant behavior corresponding to phases i and ii, although further studies are required in order to determine the source of the discrepancy between our method and FHJ's approach.

The perfectly symmetric initial conditions used above are somewhat artificial, and will never actually occur in a real flow. It is for this reason that we also simulated the asymmetric initial configuration pictured in Fig. 15(d) with particles at locations $x=\frac{L_x}{2}-\frac{W}{4}$ and $\frac{L_x}{2}$. Otherwise, the channel width W=$8D$ and Reynolds number Re=4.4 remain the same as in the symmetric case. Numerical results are shown in Figs. 28 and 30 where the particles exhibit similar dynamics to the symmetric case and approach the same steady state solution. The only difference appears in the transient motion where the particles undergo one additional horizontal oscillation en route to steady state.

https://doi.org/10.4208/cicp.061113.050115a Published online by Cambridge University Press

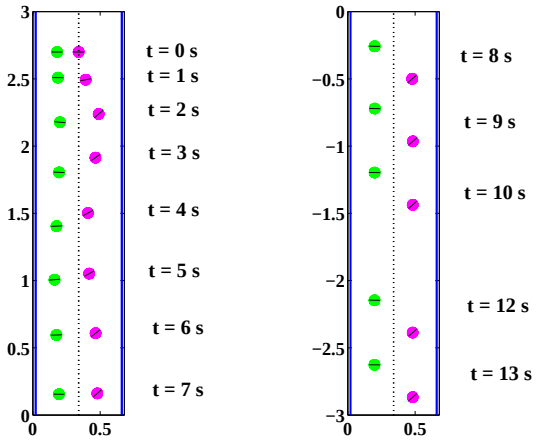


Figure 30: Snapshots of interactions for two particles initially aligned horizontally and off-center. Parameter values: $W=8D$ and $Re=4.4$.

6 Conclusions

The main aim of this paper was to demonstrate the ability of the immersed boundary method to simulate realistic dynamics of solid particles settling under gravity within a Newtonian incompressible fluid. The particles are modelled as a network of stiff springs and the added mass of the particles is incorporated using a gravitational forcing term that is spread onto fluid points via a regularized delta function. Numerical simulations of a single particle show excellent agreement with the best available empirical formula for wall-corrected settling velocity due to Faxén as well as with the drag coefficient from experiments and other numerical simulations. Furthermore, long-time simulations of two particles reproduce the qualitative features of the dynamics observed in both experiments and other numerical simulations.

This study is by no means a comprehensive comparison to other results from the extensive literature on particle sedimentation, but rather sets the stage for such a study in future. In particular, we plan to perform a more detailed comparison with other published results, focusing first on our idealized cylindrical particles. By implementing improvements to the numerical algorithm that increase accuracy of the solution approximation (such as in [33]), we hope to be able to explain the discrepancy we observed between our results and those of Feng, Hu and Joseph [18]. After that, the natural next step would be to extend our numerical method to 3D in order to permit simulations spherical particle interactions in a more realistic geometry.

We emphasize that this study is a "proof-of-concept" that the immersed boundary method is capable of simulating the sedimentation of particles that are denser than the suspending fluid. We make no claim to improve on or to compete with other numerical methods that are specially-tailored to deal with rigid, non-deformable particles. In-

https://doi.org/10.4208/cicp.061113.050115a Published online by Cambridge University Press

stead, our ultimate goal is to solve sedimentation problems involving irregularly-shaped and highly deformable particles, which to our knowledge has not been sufficiently well studied in the literature. Such particle systems arise in the study of suspensions of red blood cells, wood pulp fibers, vesicles, bubbles, etc. Making use of the uniform triangulated meshes from the DistMesh package will allow us to deal with more general particle shapes. Since the Boussinesq approximation employed in our model for handling added mass restricts the applicability to low Reynolds numbers, we plan in future to implement the penalty IB method of Kim and Peskin [30] which has no such restriction. Furthermore, we will make use of recent developments in massively parallel immersed boundary algorithms by Wiens and Stockie [51], which should prove instrumental in permitting efficient IB simulations of non-dilute suspensions containing large numbers of particles, especially in three dimensions.

Acknowledgments

This work was supported by grants from the Natural Sciences and Engineering Research Council of Canada and the Mprime Network of Centres of Excellence.

References

[1] C. K. Aidun and E.-J. Ding. Dynamics of particle sedimentation in a vertical channel: Period-doubling bifurcation and chaotic state. *Phys. Fluids*, 15(6):1612–1621, 2003.
[2] E. Alpkvist and I. Klapper. Description of mechanical response including detachment using a novel particle model of biofilm/flow interaction. *Water Sci. Tech.*, 55:265–273, 2007.
[3] G. K. Batchelor. *An Introduction to Fluid Dynamics*. Cambridge University Press, 1967.
[4] A. Ben Richou, A. Ambari, M. Lebey, and J. K. Naciri. Drag force on a circular cylinder midway between two parallel plates at $Re \ll 1$. Part 2: moving uniformly (numerical and experimental). *Chem. Eng. Sci.*, 60(10):2535–2543, 2005.
[5] A. P. S. Bhalla, R. Bale, B. E. Griffith, and N. A. Patankar. A unified mathematical framework and an adaptive numerical method for fluid-structure interaction with rigid, deforming, and elastic bodies. *J. Comput. Phys.*, 250:446–476, 2013.
[6] D. Boffi, L. Gastaldi, and L. Heltai. On the CFL condition for the finite element immersed boundary method. *Comput. Struct.*, 85:775–783, 2007.
[7] H. Brenner. Hydrodynamic resistance of particles at small Reynolds number. *Adv. Chem. Eng.*, 6:287–438, 1966.
[8] W.-P. Breugem. A second-order accurate immersed boundary method for fully resolved simulations of particle-laden flows. *J. Comput. Phys.*, 231(13):4469–4498, 2012.
[9] T. T. Bringley. *Analysis of the Immersed Boundary Method for Stokes Flow*. PhD thesis, Department of Mathematics, New York University, May 2008.
[10] R. Bürger and W. L. Wendland. Sedimentation and suspension flows: Historical perspective and some recent developments. *J. Eng. Math.*, 41:101–116, 2001.
[11] S. Champmartin and A. Ambari. Kinematics of a symmetrically confined cylindrical particle in a "Stokes-type" regime. *Phys. Fluids*, 19:073303, 2007.

https://doi.org/10.4208/cicp.061113.050115a Published online by Cambridge University Press

[12] Y. Cheng, L. Zhu, and C. Zhang. Numerical study of stability and accuracy of the immersed boundary method coupled to the lattice Boltzmann BGK model. *Commun. Comput. Phys.*, 16(1):136–168, 2014.
[13] R. P. Chhabra, S. Agarwal, and K. Chaudhary. A note on wall effect on the terminal falling velocity of a sphere in quiescent Newtonian media in cylindrical tubes. *Powder Tech.*, 129:53–58, 2003.
[14] R. H. Davis and A. Acrivos. Sedimentation of noncolloidal particles at low Reynolds numbers. *Annu. Rev. Fluid Mech.*, 17:91–118, 1985.
[15] R. Di Felice. The sedimentation velocity of dilute suspensions of nearly monosized spheres. *Int. J. Multiphase Flow*, 25:559–574, 1999.
[16] A. Dupuis, P. Chatelain, and P. Koumoutsakos. An immersed boundary-lattice-Boltzmann method for the simulation of the flow past an impulsively started cylinder. *J. Comput. Phys.*, 227(9):4486–4498, 2008.
[17] O. H. Faxén. Forces exerted on a rigid cylinder in a viscous fluid between two parallel fixed planes. *Proc. Roy. Swed. Acad. Sci.*, 187:1–13, 1946.
[18] J. Feng, H. H. Hu, and D. D. Joseph. Direct simulation of initial value problems for the motion of solid bodies in a Newtonian fluid. Part 1. Sedimentation. *J. Fluid Mech.*, 261:95–134, 1994.
[19] A. F. Fortes, D. D. Joseph, and T. S. Lundgren. Nonlinear mechanics of fluidization of beds of spherical particles. *J. Fluid Mech.*, 177:467–483, 1987.
[20] S. Ghosh. *The immersed boundary method for simulating gravitational settling and fluid shear-induced deformation of elastic structures*. PhD thesis, Department of Mathematics, Simon Fraser University, Burnaby, Canada, Mar. 2013. Available at `http://summit.sfu.ca/item/12775`.
[21] R. Glowinski, T. W. Pan, T. I. Hesla, D. D. Joseph, and J. Périaux. A fictitious domain approach to the direct numerical simulation of incompressible viscous flow past moving rigid bodies: Application to particulate flow. *J. Comput. Phys.*, 169(2):363–426, 2001.
[22] B. E. Griffith, R. D. Hornung, D. M. McQueen, and C. S. Peskin. An adaptive, formally second order accurate version of the immersed boundary method. *J. Comput. Phys.*, 223(1):10–49, 2007.
[23] S. Haeri and J. S. Shrimpton. On the application of immersed boundary, fictitious domain and body-conformal mesh methods to many particle multiphase flows. *Int. J. Multiphase Flow*, 40:38–55, 2012.
[24] J. Happel and H. Brenner. *Low Reynolds number hydrodynamics, with special applications to particulate media*. Mechanics of fluids and transport processes. M. Nijhoff Publishers, 1983.
[25] J. P. Hernández-Ortiz. *Boundary Integral Equations for Viscous Flows — non-Newtonian Behavior and Solid Inclusions*. PhD thesis, Department of Mechanical Engineering, University of Wisconsin-Madison, 2004.
[26] M. M. Hopkins and L. J. Fauci. A computational model of the collective fluid dynamics of motile microorganisms. *J. Fluid Mech.*, 455:149–174, 2002.
[27] H. H. Hu, D. D. Joseph, and A. F. Fortes. Experiments and direct simulation of fluid particle motions. *Int. Vid. J. Eng. Res.*, 2:17–24, 1997.
[28] K. O. L. F. Jayaweera and B. J. Mason. The behaviour of freely falling cylinders and cones in a viscous fluid. *J. Fluid Mech.*, 22(4):709–720, 1965.
[29] D. D. Joseph, A. Fortes, T. S. Lundgren, and P. Singh. Nonlinear mechanics of fluidization of spheres, cylinders and disks in water. In *Advances in Multiphase Flow and Related Problems*, pages 101–122. SIAM, Philadelphia, PA, 1987.
[30] Y. Kim and C. S. Peskin. Penalty immersed boundary method for an elastic boundary with

https://doi.org/10.4208/cicp.061113.050115a Published online by Cambridge University Press

mass. *Phys. Fluids*, 19(5):053103, 2007.
[31] A. J. C. Ladd. Numerical simulations of particulate suspensions via a discretized Boltzmann equation. Part II. Numerical results. *J. Fluid Mech.*, 271:311–339, 1994.
[32] M.-C. Lai. *Simulations of the flow past an array of circular cylinders as a test of the immersed boundary method*. PhD thesis, New York University, Sept. 1998.
[33] M.-C. Lai and C. S. Peskin. An immersed boundary method with formal second-order accuracy and reduced numerical viscosity. *J. Comput. Phys.*, 160(2):705–719, 2000.
[34] R. Mittal and G. Iaccarino. Immersed boundary methods. *Annu. Rev. Fluid Mech.*, 37:239–261, 2005.
[35] R. Münster, O. Mierka, and S. Turek. Finite element-fictitious boundary methods (FEM-FBM) for 3D particulate flow. *Int. J. Numer. Meth. Fluids*, 69(2):294–313, 2012.
[36] P. O. Persson and G. Strang. A simple mesh generator in MATLAB. *SIAM Review*, 46(2):329–345, 2004.
[37] C. S. Peskin. The immersed boundary method. *Acta Numer.*, 11:1–39, 2002.
[38] N. Phan-Thien and X.-J. Fan. Viscoelastic mobility problem using a boundary element method. *J. Non-Newton. Fluid Mech.*, 105(2-3):131–152, 2002.
[39] G. Pianet and E. Arquis. Simulation of particles in fluid: a two-dimensional benchmark for a cylinder settling in a wall-bounded box. *Euro. J. Mech. B Fluids*, 27:309–321, 2008.
[40] J. F. Richardson and W. N. Zaki. Sedimentation and fluidisation: Part I. *Trans. Inst. Chem. Eng.*, 32:35–53, 1954.
[41] J. M. Stockie. *Analysis and Computation of Immersed Boundaries, with Application to Pulp Fibres*. PhD thesis, Institute of Applied Mathematics, University of British Columbia, Vancouver, Canada, 1997. Available at `http://circle.ubc.ca/handle/2429/7346`.
[42] J. M. Stockie. Modelling and simulation of porous immersed boundaries. *Comput. Struct.*, 87(11-12):701–709, 2009.
[43] G. G. Stokes. Section IV. Determination of the motion of a fluid about a sphere which moves uniformly with a small velocity. In *Mathematical and Physical Papers*, volume III of *The Sources of Science, No. 33*, pages 55–67. Cambridge University Press, Teddington, UK, second edition, 1966. First published in 1901.
[44] D. Sucker and H. Brauer. Fluiddynamik bei quer angeströmten Zylindern. *Heat Mass Transfer*, 8(3):149–158, 1975.
[45] Y. Takaisi. The drag on a circular cylinder moving with low speeds in a viscous liquid between two parallel walls. *J. Phys. Soc. Japan*, 10:685–693, 1955.
[46] M. Uhlmann. An immersed boundary method with direct forcing for the simulation of particulate flows. *J. Comput. Phys.*, 209:448–476, 2005.
[47] P. Vasseur and R. G. Cox. The lateral migration of spherical particles sedimenting in a stagnant bounded fluid. *J. Fluid Mech.*, 80(3):561–591, 1977.
[48] J. Wang and A. Layton. Numerical simulations of fiber sedimentation in Navier-Stokes flow. *Commun. Comput. Phys.*, 5(1):61–83, 2009.
[49] Z. Wang, J. Fan, and K. Luo. Combined multi-direct forcing and immersed boundary method for simulating flows with moving particles. *Int. J. Multiphase Flow*, 34:283–302, 2008.
[50] C. M. White. The drag of cylinders in fluids at slow speeds. *Proc. Roy. Soc. A*, 186:472–479, 1946.
[51] J. K. Wiens and J. M. Stockie. An efficient parallel immersed boundary algorithm using a pseudo-compressible fluid solver. *J. Comput. Phys.*, 281:917–941, 2015.
[52] L. Zhu and C. S. Peskin. Simulation of a flapping flexible filament in a flowing soap film by the immersed boundary method. *J. Comput. Phys.*, 179(2):452–468, 2002.

https://doi.org/10.4208/cicp.061113.050115a Published online by Cambridge University Press